Navier-Stokes–based linear model for unstably stratified turbulent channel flows

Anagha Madhusudanan,[1,2,*] Simon J. Illingworth,[1] Ivan Marusic [ORCID],[1] and Daniel Chung [ORCID][1]

[1]*Department of Mechanical Engineering, University of Melbourne, Victoria 3010, Australia*
[2]*Graduate Aerospace Laboratories, California Institute of Technology, Pasadena, California 91125, USA*

We use the linearized Navier-Stokes equations to study the large-scale flow structures in unstably stratified turbulent channel flows. The impulse response of the linear operator at bulk Richardson numbers from $\mathrm{Ri}_b = 0.001$ to $\mathrm{Ri}_b = 1.0$ are considered, corresponding to the increasing influence of buoyancy relative to shear. We compare the streamwise-constant flow structures predicted by the linear model to the quasistreamwise rolls that emerge with increasing Ri_b in direct numerical simulations (DNSs) [e.g., Pirozzoli *et al.*, J. Fluid Mech. **821**, 482 (2017)]. The linearized Navier-Stokes equations augmented with eddy-viscosity and eddy-diffusivity capture the emergence of the quasistreamwise rolls well. With increasing Ri_b, the temperature fluctuations of the streamwise-constant flow structures transition from having a peak in intensity at the channel centerline to having two peaks, one at each wall, consistent with DNS.

I. INTRODUCTION

Streamwise-elongated large-scale flow structures are ubiquitous in wall-bounded shear flows, and they play a significant role in the transport of momentum within these flows (e.g., Refs. [1–15]). Hence a number of studies have concentrated on modeling these structures (e.g., Refs. [16–24]). In addition to shear, buoyancy can also play an active role. Direct numerical simulations (DNSs) in which both shear and buoyancy are active have revealed that large-scale flow structures are also present in these flows, and they impact the transport of heat and momentum within the flow (e.g., Refs. [25–28]). An example of such flow structures in atmospheric flows are streets of cumulus clouds (e.g., Refs. [29–31]). The modeling of the large-scale structures in these flows have received less attention. Hence in the current work we use a linearized Navier-Stokes–based model to investigate the flow structures that emerge from competing shear-driven and buoyancy-driven mechanisms in fully turbulent unstably stratified channel flows.

Linear analysis of the Navier-Stokes equations has shown that the streamwise-constant structures are the most amplified features in turbulent wall-bounded flows (e.g., Refs. [16–18,20,21]). Recently, Illingworth [32] used a linear analysis to show that Couette flow can efficiently leverage the mean wall-normal shear to produce channelwide streamwise-constant rolls, consistent with DNS and experiments [33–42]. In the case of unstably stratified channel flows, Jerome *et al.* [43] analyzed the linearized Navier-Stokes equations in the laminar regime. They showed that the streamwise-constant structures are again the most amplified features and that these features are sensitive to buoyancy.

Such streamwise-constant flow structures also appear in unstably stratified turbulent flows as seen in direct numerical simulations of Pirozzoli *et al.* [25] and Blass *et al.* [26]. Let us concentrate
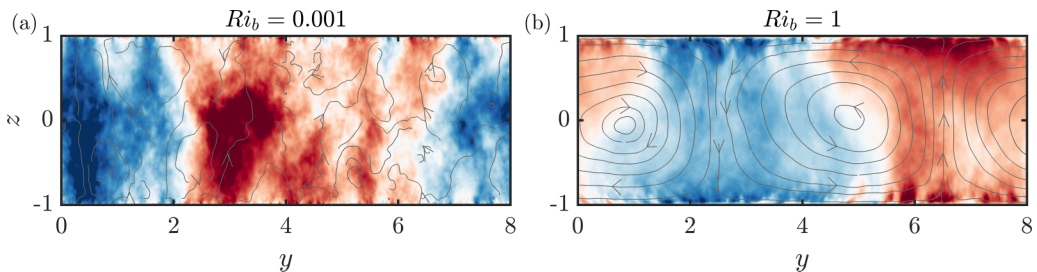
---

*anaghamadhu91@gmail.com

FIG. 1. Data from Pirozzoli *et al.* [25]. Streamwise-averaged temperature fluctuations (contours) and cross-stream velocities (streamlines) in the spanwise wall-normal plane at bulk Richardson numbers (a) $Ri_b = 0.001$ and (b) $Ri_b = 1.0$. These figures correspond to Figs. 5(j) and 5(f) from Pirozzoli *et al.* [25]. Negative values are shown in blue and the positive values in red. The spanwise *y* and the wall-normal *z* coordinates have been nondimensionalized by the channel half-width.

on the direct numerical simulation dataset of Pirozzoli *et al.* [25]. They considered a turbulent channel flow and heated the bottom wall and cooled the top wall, thereby introducing unstable stratification into the flow. Where the effect of buoyancy relative to shear was low, they observed large-scale flow structures in temperature, but no discernible large-scale pattern in the cross-stream velocity fields [see Fig. 5(j) of Pirozzoli *et al.* [25] shown here in Fig. 1(a)]. As they increased the effect of buoyancy, channelwide rollers emerged, with two peaks in the intensity of temperature fluctuations, one at each wall [see Fig. 5(f)5 of Pirozzoli *et al.* [25] shown here in Fig. 1(b)]. These peaks correspond to the plume-ejecting region on one wall, and the corresponding plume-impacting region directly opposite to it on the second wall, that were identified in turbulent Rayleigh-Bénard flows [44,45]. Within unstably stratified channel flows, these two-peaked intensity features are also as long as the channel length (see Fig. 3(f) of Pirozzoli *et al.* [25], not shown here). Hence the DNS study of Pirozzoli *et al.* [25] showed that we obtain streamwise-constant channelwide two-peaked intensity features as we increase the effect of buoyancy in unstably stratified turbulent channel flows, and these are the quasistreamwise rolls of these flows.

In the current work we build a linearized Navier-Stokes–based model for unstably stratified turbulent channel flows. We consider bulk Richardson numbers (Ri_b) from 0.001 to 1.0 ($Ri_b = 2\beta g \Delta\theta h/u_b^2$ indicates the relative importance of buoyancy and shear, and is defined using the thermal expansion coefficient β, the acceleration due to gravity g, temperature difference $\Delta\theta$ maintained across the walls, the channel half-height h and the bulk velocity u_b). The aim is to understand to what extent the model can capture the quasistreamwise rolls observed in these flows. There are many techniques that can be used to analyze the linearized Navier-Stokes equations. For instance, the resolvent analysis framework (e.g., Refs. [19,21,46,47]) or the stochastically forced operator (e.g., Refs. [20,21,48,49]) can be used. In both these cases the forcing to the linear model is considered to be a superposition of Fourier modes in the streamwise and the spanwise directions. In the case of the resolvent analysis, the forcing is also taken to be a superposition of Fourier modes in time, while for the stochastically forced operator a random forcing in time and in the wall-normal direction is assumed. The resolvent analysis framework has been used to study passive scalar transport [50–52], and recent work by Ahmed *et al.* [53] extended this framework to study stably stratified turbulent flows. An alternative technique that can be used to analyze the linear operator is to consider its impulse response, where the forcing is taken to be a superposition of impulses in space and time. In this approach we do not choose the Fourier mode to analyze and instead choose the location of the impulse in space and time. For the case of the quasistreamwise rolls that we are interested in, from DNS we know that these structures have length scales comparable to the channel length [25] and we can therefore concentrate on the streamwise-constant structures to model them. In contrast, it would be interesting to analyze these structures without *a priori* selecting their spanwise length scales or their temporal frequencies. We therefore use the impulse response of

the linear operator to study these structures, thereby eliminating the requirement to *a priori* choose a spanwise wavelength or a temporal frequency.

In one of the earliest works on the impulse response of the linearized equations, Huerre and Monkewitz [54] used the response to distinguish between absolutely unstable and convectively unstable flows. Jovanović and Bamieh [55] and Jovanović [56] considered the impulse response in the context of laminar channel flows, and they were able to show that streamwise streaks, similarly to those experimentally observed in both transitional and fully turbulent flows, emerged as the dominant response to the impulse. Hariharan *et al.* [57] extended this analysis technique to study viscoelastic fluids. In a related but different approach, Luchini *et al.* [58] and Codrignani [59] analyzed the response of a fully developed turbulent channel flow to impulsive forcing, with the goal of developing control strategies based on the observed responses. Of more direct relevance to the current work is the study by Vadarevu *et al.* [60] where they showed that the impulse response of the linearized Navier-Stokes equations for a turbulent channel flow predicts wall-attached self-similar structures, consistent with the observations from experiments. In the current work, to analyze the linear model for an unstably stratified turbulent channel flow, we compute its response to an impulse located at a streamwise and spanwise location (0,0) and at some prescribed wall-normal location and study the response as a function of time. We will see that, as observed in the DNS study of Pirozzoli *et al.* [25], the relative effect of shear and buoyancy in the model, characterized by the Richardson number Ri_b, has a significant impact on the predicted coherent structures.

The outline of the paper is as follows. The linearized Navier-Stokes–based model for unstably stratified turbulent channel flows is described in Sec. II. Details concerning the calculation of the impulse response is given in Sec. III, and the coherent flow structures that appear in these impulse responses are shown in Sec. IV. In Sec. V the impact of varying the influence of buoyancy relative to shear on these structures is considered. Further, in Sec. VI the model is used to compute the mean temperature variance profiles as a function of Ri_b, which are then used to provide a more direct comparison of the model with DNS. We will see that the streamwise-constant linearized Navier-Stokes equations capture pertinent features of the quasistreamwise rolls in unstably stratified turbulent channel flows. In Sec. VII the role of the streamwise-varying modes on the modeling of the quasistreamwise rolls is discussed and in Sec. VIII we consider the influence of changing the impulse location relative to the wall. We briefly analyze the role of the different components of the linear model in capturing these flow structures in Sec. IX, which is then followed by a summary of the results in Sec. X.

II. LINEAR MODEL

A statistically steady, incompressible turbulent channel flow is considered, with the streamwise, spanwise, and wall-normal directions denoted by x, y, and z, respectively, and the corresponding velocity components by u, v, and w. The temperature is denoted by θ. A temperature difference $\Delta\theta$ maintained across the walls gives rise to unstable stratification. Velocities are normalized by the friction velocity $u_\tau = \sqrt{(\tau_w/\rho)}$, where τ_w is the wall shear stress and ρ is the density. The spatial variables are normalized by the channel half-height h and the temperature by $\Delta\theta$. The nondimensional channel half-height is therefore unity. The pressure fluctuations p are normalized by ρu_τ^2.

The nondimensional numbers that define the problem are (i) the bulk Reynolds number $\mathrm{Re}_b = 2hu_b/\nu$ where ν is the kinematic viscosity, (ii) the Rayleigh number $\mathrm{Ra} = (8\beta g\Delta\theta h^3)/(\alpha\nu)$ where α is the thermal diffusivity, and (iii) the Prandtl number $\mathrm{Pr} = \nu/\alpha$. These nondimensional numbers are used to define a bulk Richardson number $\mathrm{Ri}_b = \mathrm{Ra}/(\mathrm{Re}_b^2\mathrm{Pr})$ that indicates the relative importance of buoyancy and shear. This Richardson number Ri_b will be used extensively in the later sections of this work as an indicator of the relative influence of buoyancy and shear. Additionally, the friction Reynolds number is defined as $\mathrm{Re}_\tau = u_\tau h/\nu$, and a corresponding friction Richardson number is
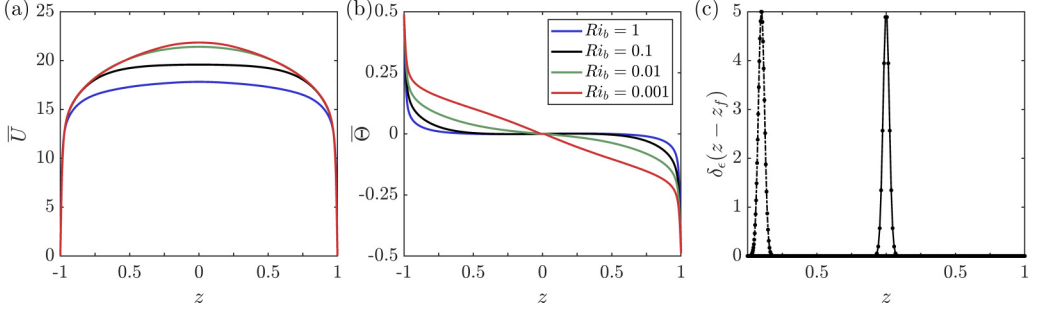
FIG. 2. (a) The mean streamwise velocity profile $\overline{U}$ and (b) the mean temperature profile $\overline{\Theta}$ from Pirozzoli *et al.* [25] that are given as inputs to the linear model. The profiles are shown for the different Richardson numbers considered in this work. The Gaussian profiles (11) used to approximate the delta functions are also shown in (c) for two impulse locations of $z_f = 0$ (solid line) and -0.9 (dashed-dotted line). The markers ($\bullet$) indicate the grid points used for discretizing the wall-normal direction.

defined as $\mathrm{Ri}_\tau = \beta g \Delta \theta h / u_\tau^2$. The equations nondimensionalized by u_τ, h, and $\Delta \theta$ are as follows:

$$
\begin{aligned}
&\frac{\partial \mathbf{u}}{\partial t} + U \frac{\partial \mathbf{u}}{\partial x} + w \frac{dU}{dz} \hat{\mathbf{i}} + \nabla p - \nabla \cdot (\nu_T \nabla \mathbf{u}) - \mathrm{Ri}_\tau \theta \hat{\mathbf{k}} = \mathbf{d}, \quad \nabla \cdot \mathbf{u} = 0, \\
&\frac{\partial \theta}{\partial t} + U \frac{\partial \theta}{\partial x} + w \frac{d\Theta}{dz} - \nabla \cdot (\alpha_T \nabla \theta) = d_\theta,
\end{aligned}
\tag{1}
$$

where $\mathbf{u} = (u, v, w)$ are the velocity fluctuations, $U(z)$ is the turbulent mean-velocity profile, and $\Theta(z)$ is the mean-temperature profile. The terms $\hat{\boldsymbol{i}}$, $\hat{\boldsymbol{j}}$, and $\hat{\boldsymbol{k}}$ denote the unit vectors along x, y, and z, respectively. It should be noted that z is the wall-normal distance measured from the channel centerline, i.e., $z = 0$ represents the channel centerline and the walls are at $z = -1$ and $z = 1$. Here $\mathbf{d} = (d_x, d_y, d_z) = -\boldsymbol{u} \cdot \nabla \boldsymbol{u} + \overline{\boldsymbol{u} \cdot \nabla \boldsymbol{u}}$ represents the nonlinear terms in the momentum equation and $d_\theta = -\boldsymbol{u} \cdot \nabla \theta + \overline{\boldsymbol{u} \cdot \nabla \theta}$ represents the nonlinear terms in the equation governing the temperature. The mean-velocity and the mean-temperature profiles required as input to the model are obtained from the DNS dataset of Pirozzoli *et al.* [25] and are shown here in Figs. 2(a) and 2(b).

From the literature we know that the linearized Navier-Stokes equations augmented with an eddy-viscosity correctly predicts the length scales of the coherent structures in turbulent wall-bounded flows without stratification [16,17,21,61]. Inspired by this, here the viscosity and the thermal diffusivity are augmented by wall-normally varying dimensionless eddy-viscosity $\nu_t(z)$ and dimensionless eddy-diffusivity $\alpha_t(z)$, respectively. Hence in (1), $\nu_T(z) = 1/\mathrm{Re}_\tau + \nu_t(z)$ and $\alpha_T(z) = 1/(\mathrm{Re}_\tau \mathrm{Pr}) + \alpha_t(z)$. The Cess [62] profile that is generally used to compute ν_T for turbulent channel flows (e.g., Refs. [17,21]) cannot accurately model ν_T for the case of a stratified turbulent channel flow. Therefore, the profiles for ν_T and α_T are computed from the mean profiles of Pirozzoli *et al.* [25] using [63]

$$
\nu_T(z) = \frac{-z}{dU/dz}, \quad \alpha_T(z) = \frac{1}{d\Theta^+/dz}.
\tag{2}
$$

Here $\Theta^+ = \Theta/(\theta_\tau/\Delta\theta)$, where the friction temperature θ_τ is given by $\theta_\tau/\Delta\theta = (\mathrm{Re}_\tau \mathrm{Pr})^{-1}(d\Theta/dz)|_{\mathrm{wall}}$. It should be noted that, although $d\Theta/dz < 0$, $(\theta_\tau/\Delta\theta)$ is also a negative quantity, thereby making $d\Theta^+/dz > 0$ and hence $\alpha_T > 0$. The computation of eddy-viscosity and eddy-diffusivity is further discussed in Sec. II B.

A. Orr-Sommerfeld-Squire form

The model in (1) can now be written in Orr-Sommerfeld Squire form [64], augmented with the equation for the temperature fluctuations. We consider $\boldsymbol{u}$, θ, $\boldsymbol{d}$, and d_θ in terms of their two-dimensional (2D) Fourier transforms in the homogeneous streamwise and spanwise directions:

$$l(x, y, z, t) = \int_{-\infty}^{\infty} \int_{-\infty}^{\infty} \hat{l}(z, t; k_x, k_y) e^{(ik_x x + ik_y y)} dk_x dk_y, \tag{3}$$

where l represents the variable $\boldsymbol{u}$, θ, $\boldsymbol{d}$, or d_θ and $\hat{\ }$ represents the Fourier transform. Here (k_x, k_y) are the streamwise and spanwise wave numbers and (λ_x, λ_y) the corresponding wavelengths. The wave numbers are nondimensionalized by $(1/h)$ and the wavelengths by h. In terms of these Fourier transforms, the Orr-Sommerfeld Squire form of the model in (1) is [43]

$$\dot{\hat{q}} = A\hat{q} + B\hat{d},$$
$$\hat{u} = C\hat{q}. \tag{4}$$

The vector $\hat{\boldsymbol{q}} = (\hat{w}, \hat{\eta}, \hat{\theta})$ is composed of the wall-normal velocity, wall-normal vorticity ($\hat{\eta} = ik_y\hat{u} - ik_x\hat{v}$), and temperature in Fourier space (it should be noted that, according to the coordinate system adopted here, $\hat{\eta}$ points in the $-z$ direction). We therefore have an additional variable, θ, when compared to the standard Orr-Sommerfeld Squire equations. The boundary conditions enforced on both walls are $\hat{w}(\pm 1) = \partial\hat{w}/\partial z(\pm 1) = \hat{\eta}(\pm 1) = \hat{\theta}(\pm 1) = 0$ (e.g., Refs. [43,65]). The definitions of the matrices A, B, and C are

$$A(k_x, k_y) = \begin{bmatrix} \Delta & 0 & 0 \\ 0 & I & 0 \\ 0 & 0 & I \end{bmatrix}^{-1} \begin{bmatrix} \mathcal{L}_{\mathcal{OS}} & 0 & -\text{Ri}_\tau\, k^2 \\ -ik_y U' & \mathcal{L}_{\mathcal{SQ}} & 0 \\ -\Theta' & 0 & \mathcal{L}_{\mathcal{SQT}} \end{bmatrix}, \tag{5}$$

$$B(k_x, k_y) = \begin{bmatrix} \Delta & 0 & 0 \\ 0 & I & 0 \\ 0 & 0 & I \end{bmatrix}^{-1} \begin{bmatrix} -ik_x\mathcal{D} & -ik_y\mathcal{D} & -k^2 & 0 \\ ik_y & -ik_x & 0 & 0 \\ 0 & 0 & 0 & 1 \end{bmatrix}, \tag{6}$$

$$C(k_x, k_y) = \frac{1}{k^2} \begin{bmatrix} ik_x\mathcal{D} & -ik_y & 0 \\ ik_y\mathcal{D} & ik_x & 0 \\ k^2 & 0 & 0 \\ 0 & 0 & k^2 \end{bmatrix}. \tag{7}$$

Here $\mathcal{D}$ and $'$ represent differentiation in the wall-normal direction, and $\Delta = \mathcal{D}^2 - k^2$ where $k^2 = k_x^2 + k_y^2$. The matrices $\mathcal{L}_{OS}$ and $\mathcal{L}_{SQ}$ in (5) are the Orr-Sommerfeld and Squire operators, respectively. The operators $\mathcal{L}_{\mathcal{OS}}$, $\mathcal{L}_{\mathcal{SQ}}$ and $\mathcal{L}_{\mathcal{SQT}}$ are defined as

$$\begin{aligned} \mathcal{L}_{\mathcal{OS}} &= -ik_x U \Delta + ik_x U'' + \nu_T \Delta^2 + 2\nu_T' \mathcal{D}\Delta + \nu_T''(\mathcal{D}^2 + k^2), \\ \mathcal{L}_{\mathcal{SQ}} &= -ik_x U + \nu_T \Delta + \nu_T' \mathcal{D}, \\ \mathcal{L}_{\mathcal{SQT}} &= -ik_x U + \alpha_T \Delta + \alpha_T' \mathcal{D}. \end{aligned} \tag{8}$$

The definitions of the operators A, B, and C closely follow the definitions of the eddy-viscosity–based operators in literature (see, for example, the operators in Refs. [21,60,66,67]). The main difference is the presence of an additional operator $\mathcal{L}_{SQT}$ that appears in A due to the equation for θ in (1). The matrices B and C also each have an additional row and column that accounts for the response in temperature θ and the additional forcing component d_θ.

B. Computation of ν_T and α_T from DNS

The computation of the eddy-viscosity and the eddy-diffusivity profiles are sensitive to any noise in the mean profiles used in (2). This is especially true when (i) the value of Ra is high and (ii) toward the channel center where the profiles of U and Θ plateau, and hence have very small derivatives,

TABLE I. The table provides the details of the four cases considered. The color scheme shown here is used throughout this paper.

	Re_b	Ra	Pr	Ri_b
——	$10^{4.5}$	10^6	1.0	0.001
——	$10^{4.5}$	10^7	1.0	0.01
——	$10^{4.5}$	10^8	1.0	0.1
——	$10^{4.5}$	10^9	1.0	1.0

as seen in Figs. 2(a) and 2(b) (that are reproductions of Figs. 12(a) and 12(b) in Pirozzoli *et al.* [25]). The profiles of ν_T and α_T can therefore become unphysical in the presence of noise in this region of the channel. (Some noise may be present since the DNS mean profiles are not always perfectly converged.) This noise is well appreciated in the atmospheric sciences, which is why the scalar-flux is modelled with a prescribed eddy-diffusivity profile in conjunction with a mass-flux plume-entrainment model (e.g., Ref. [68]).

To avoid this problem of working with unphysical viscosity and diffusivity profiles, here we use the method of interpolating the profiles used by Cossu *et al.* [18] for the case of a boundary layer. For this purpose, we construct the profiles of ν_T and α_T using the mean profiles obtained from DNS up to some specified wall-normal distance z^* measured from the channel centerline. To obtain the profiles in the remaining regions $-z^* < z < z^*$ we use linear interpolation. This is equivalent to setting the value of ν_T and α_T constant in the region $-z^* < z < z^*$. The value of z^* is chosen so as to avoid evaluating (2) in the region where the derivatives of U and Θ are too small. For the purposes of this work ν_T and α_T are constructed for four cases with different Ri_b (the parameters for these cases are shown in Table I). The profiles of ν_T for all four cases are computed with $z^* = 0.05$. That is, to compute ν_T we use interpolation only very close to the channel centerline where dU/dz goes to zero. For the case of α_T we choose $z^* = 0.5$, thereby considerably extending the interpolated region. In other words, α_T is assumed to be constant between $-0.5 < z < 0.5$. In Appendix C we look at the effect of this choice on the results obtained and thereby show that the conclusions derived here remain largely unaffected if $z^* \geqslant 0.3$. We also consider the linear model with a constant eddy-diffusivity profile α_T in Appendix A, and show that this assumption cannot be used to model the quasistreamwise rolls.

III. COHERENT FLOW STRUCTURES FROM THE IMPULSE FORCING

We now assess the linear model's ability to capture the quasistreamwise rolls observed in the DNS of unstably stratified channel flows [25,26]. By the very definition of these structures we know that only the largest streamwise length scales are important for their modeling, and we therefore choose to analyze only these scales. In contrast, it would be convenient not to choose *a priori* the spanwise length scales or the temporal frequencies of these structures. Vadarevu *et al.* [60] looked at the impulse response of the linearized Navier-Stokes equations for the flow in a turbulent channel, thereby removing this requirement to select a Fourier mode to analyze. To study the linear model for unstably stratified turbulent channel flows, we therefore compute the response of the linear operator (4) to impulsive forcing. In this case an impulse in physical space is used to force the linearized equations and the response to this impulse is computed.

To compute this impulse response, an impulse centered at a wall-normal location z_f is introduced in the linearized equations at $x = y = t = 0$. The spatiotemporal impulse is denoted by a Dirac delta function $\delta(\boldsymbol{x} - \boldsymbol{x}_0, t)$. This impulse can be factored into impulses in x, y, z, and t, i.e.,

$$\delta(\boldsymbol{x} - \boldsymbol{x}_0, t) = \delta(x)\delta(y)\delta(z - z_f)\delta(t). \tag{9}$$

A Fourier decomposition of $\delta(\boldsymbol{x} - \boldsymbol{x}_0, t)$ in x and y gives Fourier transforms of equal magnitude for all k_x and k_y. Hence (4) can now be written as

$$\dot{\hat{q}} = A\hat{q} + B\hat{d}\delta(t),$$
$$\hat{u} = C\hat{q}. \tag{10}$$

where $\hat{\boldsymbol{d}}(z) = [m_x\delta(z - z_f), m_y\delta(z - z_f), m_z\delta(z - z_f), m_\theta\delta(z - z_f)]$. The values of m_x, m_y, m_z, and m_θ set the amplitude of the forcing (independent of k_x and k_y) in each direction. The delta function in the wall-normal direction is approximated by a Gaussian function of the form

$$\delta_\epsilon(z - z_f) \equiv K \exp\left[-\frac{(z - z_f)^2}{\epsilon^2}\right]. \tag{11}$$

The value of z_f sets the wall-normal location at which the impulse is centered and ϵ sets the width of the impulse which is here taken to be constant independent of z_f and $\epsilon^2 = 10^{-3}$ (ϵ is set large enough such that there is a sufficient number of grid points to resolve the Gaussian at the channel centerline, where the density of the grid points is the minimum on the Chebyshev grid used to discretize the wall-normal direction). Figure 2(c) shows the Gaussian profiles (along with the grid points used to resolve them) used to approximate the two impulses, one at $z_f = 0$ and the other at $z_f = -0.9$, that are used in this work. We have confirmed that decreasing this value of ϵ does not have any significant impact on the results obtained here. The constant K is chosen such that the area under the Gaussian function (11) is unity. To compute the impulse response, the code developed by Vadarevu et al. [60] has been modified to include the effect of stratification (1).

The response to the forcing $\hat{\boldsymbol{d}}(z)$ at each time t can be calculated (independently of all other times) using the matrix exponential:

$$\hat{u}(z, t) = C e^{At} B\hat{d}(z). \tag{12}$$

Since the model (1) is linear, the impulse response can be computed independently for each streamwise and spanwise wave number of interest. An inverse Fourier transform is then used to obtain the three-dimensional velocity and temperature fields of the response at different time instances $t > 0$. The responses are computed for time instances between t of 0.1 and 8 in increments of 0.05. The wall-normal direction is discretized using a Chebyshev grid with $N = 302$ grid points. Convergence has been verified by reproducing the results with more than double the number of grid points.

A. Impulse response of $k_x = 0$ modes

Since the flow structures of interest are quasistreamwise rolls that have streamwise extents comparable to the length of the channel, it would be interesting to determine if these quasistreamwise rolls can be modelled using the streamwise-constant ($k_x = 0$) modes alone. Therefore in this work we use the impulse response of the streamwise-constant modes to model these structures. In Sec. VII it is shown that including streamwise-varying ($k_x \neq 0$) modes does not have a significant impact on the trends discussed here. We consider a spanwise domain size of 3π, with spanwise Fourier modes varying in integer multiples of $k_{y0} = 2/3$. The spanwise Fourier modes are further truncated such that $0 \leqslant k_y \leqslant 60k_{y0}$ ($\pi/20 \approx 0.15 \leqslant \lambda_y < \infty$). At the time instances that we consider here, the excluded larger wave numbers (corresponding to the smallest structures) contribute less than 0.1% of the energy of the most energetic streamwise-constant Fourier mode in the impulse response.

In Sec. V the coherent structures observed in these impulse responses are characterized for four different values of $\mathrm{Ri}_b = 0.001$, 0.01, 0.1, and 1.0, with $\mathrm{Re}_b = 10^{4.5}$ and $\mathrm{Pr} = 1$ fixed (Table I). The impulse location z_f is set to be the channel centerline (i.e., $z_f = 0$), where the influence of buoyancy-driven mechanisms (relative to shear-driven mechanisms) reach their maximum [63]. Before analyzing the model at different Ri_b, in Sec. IV we first consider a fixed $\mathrm{Ri}_b = 0.1$, and look at the response obtained from the four different components of the impulse $\boldsymbol{d}(z)$ in (1).
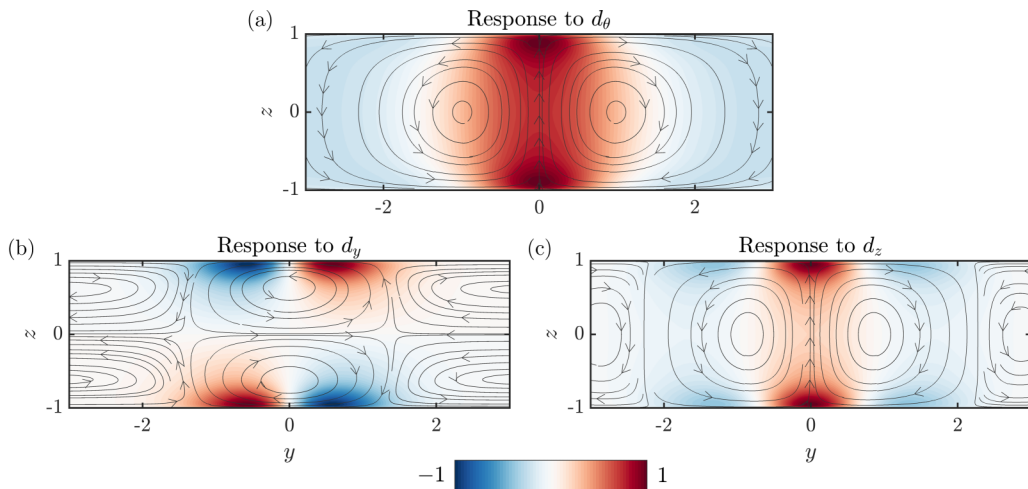
FIG. 3. The response of the streamwise constant modes ($k_x = 0$) to an impulse at $(x, y, z, t) = (0, 0, 0, 0)$ for the case of $\mathrm{Ri}_b = 0.1$ computed at time $t = 1.0$. Normalized (by the maximum) temperature fluctuations θ (contours) and cross-stream velocity components v and w (streamlines) are shown. (The streamwise component of the velocity u is not shown.) Three components of forcing are considered: (*a*) d_θ, (*b*) d_y, and (*c*) d_z. The component d_x does not force a response in temperature for streamwise-constant ($k_x = 0$) modes (see Sec. IV). The red and blue contours represent positive and negative temperature fluctuations, respectively.

IV. THE RESPONSE TO $d_x, d_y, d_z,$ AND d_θ

In this section we first consider the case of $\mathrm{Ri}_b = 0.1$ and compute the response to an impulse centered at the channel centerline ($z_f = 0$). The effects of changing Ri_b and z_f are discussed in Sec. V and Sec. VIII, respectively. There are four components of the impulse $\boldsymbol{d}(z)$ in (10): d_θ, d_x, d_y, and d_z. Rather than look at an arbitrary superposition of responses to the four components of the impulse, here we consider each forcing component separately.

Let us first concentrate on a forcing in the streamwise direction d_x. For streamwise-varying ($k_x \neq 0$) modes, d_x induces a response in the wall-normal velocity w through the nonzero term $-ik_x\mathcal{D}$ in the matrix $\boldsymbol{B}$ in (6) [row 1, column 1 in (6)]. This response in w further feeds back onto the temperature fluctuations because of the nonzero term $-\Theta'$ in the matrix $\boldsymbol{A}$ in (5) [row 3, column 1 in (5)]. Now consider the case of the streamwise-constant ($k_x = 0$) modes, which are what we are interested in here. In this case the term $-ik_x\mathcal{D}$ in $\boldsymbol{B}$ is zero, and therefore d_x does not produce a response in w. This in turn means that d_x does not effect the temperature fluctuations. In short, for streamwise-constant modes, the streamwise component of the forcing d_x does not produce a response in the temperature fluctuations. This therefore indicates that, when using the streamwise-constant model, d_x cannot model the quasistreamwise rolls that are characterized by the two peaks in intensity in the wall-normal distributions of their temperature fluctuations. The forcing d_x is therefore not considered further.

Figure 3 shows the response obtained from the other three components of forcing: d_θ, d_y, and d_z. The figure shows the temperature fluctuations θ (contours) and the cross-stream velocity components v and w (streamlines) along a wall-perpendicular plane. Let us first consider the response to d_θ shown in Fig. 3(a). From the streamlines we observe the presence of channelwide rolls. Additionally, the temperature fluctuations associated with these rolls are channelwide and have two peaks that are located close to the walls. These rolls are reminiscent of the quasistreamwise rolls observed in DNS. Now consider the response to d_z in Fig. 3(c). As in the case of the response to d_θ, we observe that d_z generates channelwide structures with two peaks in the intensity of temperature fluctuations that are located close to the walls.

Finally consider Fig. 3(b) which plots the response to d_y. From the streamlines in this figure, we observe that the response is coherent only across one half of the channel height, with the temperature fluctuations changing sign across the channel centerline. Hence these structures are not channelwide. From matrix $\boldsymbol{B}$ in (6), we note that the derivative of d_y is what effects the response in the wall-normal velocity w [row 1 column 2 in (6)]. This response in w in turn effects the response in temperature θ through the matrix $\boldsymbol{A}$ (5) [row 3, column 1 in (5)]. The derivative of an impulse localized at a wall-normal location z_f is antisymmetric with respect to this wall-normal location z_f [69]. The derivative of d_y is therefore antisymmetric with respect to the impulse location, which in Fig. 3 is the channel centerline. This therefore explains why the response in Fig. 3(b) is antisymmetric with respect to the channel centerline. It should be possible to consider a superposition of impulses for d_y that may model the quasistreamwise rolls of this flow. However, this complicates the model used here, and is therefore left as a topic for future investigation.

We can therefore make two conclusions: (i) The response of streamwise-constant modes to an impulse d_x and d_y does not faithfully model the large-scale channelwide structures in unstably stratified turbulent channel flows and (ii) the responses to d_θ and d_z show qualitative agreement with DNS. We therefore concentrate on the responses of the linear model to d_θ and d_z in the remaining sections.

V. EFFECT OF RICHARDSON NUMBER

In the previous section we considered the impulse response at a fixed Ri_b. Now we analyze the effect of varying Ri_b on the impulse response. In other words, we would like to characterize the influence of buoyancy on the structures obtained and thereby assess the model's ability to capture the flow structures that emerge from the competition of shear-driven and buoyancy-driven mechanisms. We consider four different values of $\mathrm{Ri}_b = 0.001$, 0.01, 0.1, and 1.0, while keeping $\mathrm{Re}_b = 10^{4.5}$ and $\mathrm{Pr} = 1$ fixed. The details of the four cases are given in Table I. As discussed in Sec. IV, the streamwise and spanwise forcing components d_x and d_y gives rise to structures that are not consistent with the quasistreamwise rolls observed in DNS. Hence we compute the responses to forcing in the scalar component d_θ and the wall-normal component d_z only. In the current section the impulse location is kept fixed throughout at $z_f = 0$ (i.e., the channel centerline).

To compare the responses across different Ri_b, we need to decide on a time $t_c(\mathrm{Ri}_b, z_f)$ at which the structures are compared. This time will be a function of both Ri_b and the forcing location z_f (which is kept constant in this section). One method to determine a suitable time would be to choose, for each Ri_b, a time based on the trends of a defined norm. For this purpose we choose the kinetic energy norm defined using $\hat{\boldsymbol{u}} = (\hat{u}, \hat{v}, \hat{w})$ as

$$\phi_{uu}(t) = \int_z \iint_{k_x} \int_{k_y} \hat{\boldsymbol{u}}^T(k_x, k_y, z) \hat{\boldsymbol{u}}^*(k_x, k_y, z) dk_x dk_y dz, \tag{13}$$

where $(\cdot)^T$ represents transpose and $(\cdot)^*$ represents complex conjugate. In Appendix B we show that other choices of norm do not significantly effect the conclusions made here. In Figs. 4(a) and 4(b) the kinetic energy norm ϕ_{uu} normalized by its maximum value in time is plotted as a function of t. The responses to d_θ and d_z are considered in Figs. 4(a) and 4(b), respectively, for all four values of Ri_b. Figures 4(c) and 4(d) show the responses that are obtained from the model that includes streamwise-varying modes ($k_x \neq 0$) and will be discussed in Sec. VII (the profiles are included here for ease of comparison later in Sec. VII).

First consider Fig. 4(a) which plots the norm ϕ_{uu} computed from the response to d_θ. For the cases with $\mathrm{Ri}_b = 0.001$, 0.01, and 0.1 the response shows transient growth before an eventual decay. In this case, the time at which the norm peaks is used as the time $t_c(\mathrm{Ri}_b, z_f)$ at which the responses are later compared in Fig. 5. When $\mathrm{Ri}_b = 1.0$ the norm follows an increasing trend. In this case, the time $t_c(\mathrm{Ri}_b, z_f)$ is taken to be the maximum time considered, i.e., $t_c(1.0, 0) = 8.0$. The trend of ϕ_{uu} computed from the response to d_z that is shown in Fig. 4(b) is slightly more complicated. The plot of ϕ_{uu} for all Ri_b first shows a decaying trend, followed by an increasing trend and then
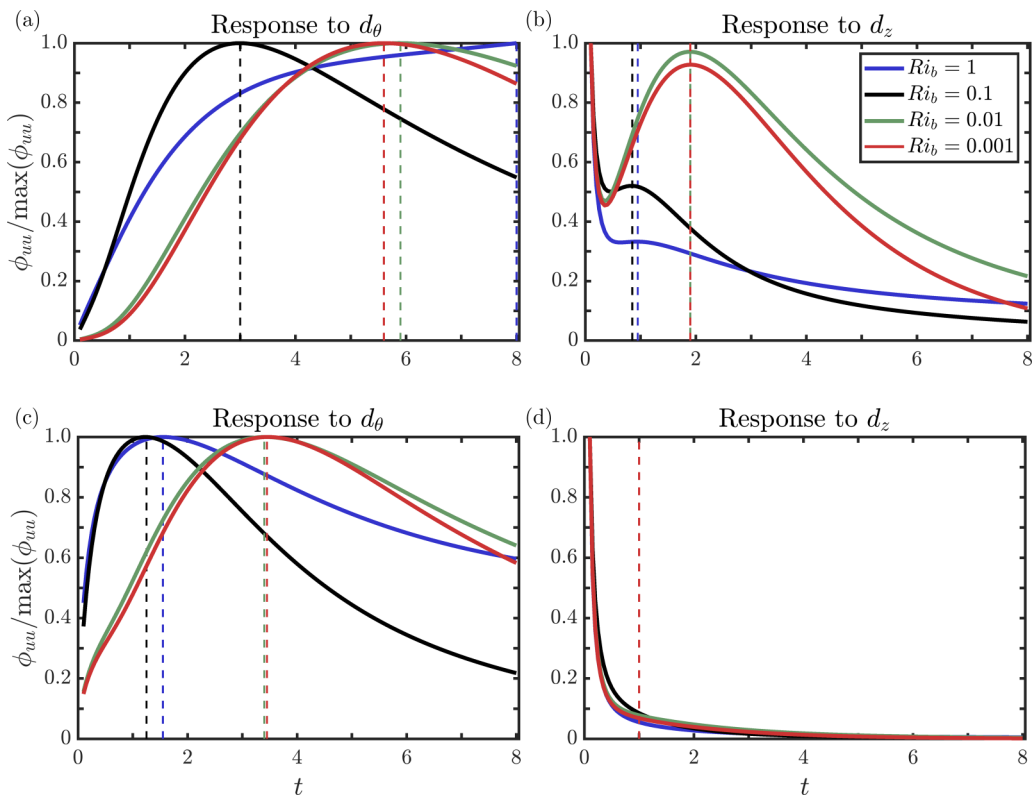
FIG. 4. The norm ϕ_{uu} obtained from the responses to an impulse located at $(x, y, z, t) = (0, 0, 0, 0)$. The norm computed from [(a) and (b)] the model including only the streamwise-constant ($k_x = 0$) modes, as well as [(c) and (d)] the model including streamwise-varying ($k_x \neq 0$) modes are shown. The norm for the response to [(a) and (c)] d_θ and [(b) and (d)] d_z are plotted as a function of t. The colors indicate four values of $Ri_b = 0.001$ (red), 0.01 (green) 0.1 (black), and 1.0 (blue). The dashed lines indicate the values of $t_c(Ri_b, z_f)$ used in Figs. 5 and 6.

again an eventual decay. This is explained by the combination of the slower transient growth in u, and the more rapid energy decay in v and w. The peak that appears after the initial decay is the time at which the transient growth in u attains a maximum, and this time is chosen as the value of $t_c(Ri_b, z_f)$ at which the responses are later compared. In general, when there is transient growth, the time at which the norms peaks is chosen as $t_c(Ri_b, z_f)$, when the norm does not show a peak we take $t_c(Ri_b, z_f) = 1.0$ and when the norm monotonically increases $t_c(Ri_b, z_f)$ is taken to be the maximum time considered.

We can now compute the response to d_θ and d_z at the times $t_c(Ri_b, z_f)$ computed from Figs. 4(a) and 4(b). This response is plotted in Fig. 5 for the four values of $Ri_b = 0.001, 0.01, 0.1,$ and 1.0. The response to d_θ is shown in the first column and the response to d_z is shown in the second column. Temperature fluctuations (contours) and the cross-stream velocity components (streamlines) along a spanwise wall-normal (y-z) plane for each Ri_b are shown. (We do not plot the streamwise velocity component in this figure. This is to enable a more direct comparison with the trends observed by Pirozzoli *et al.* [25].)

Let us first consider the response to d_θ. The value of Ri_b, and hence the effect of buoyancy, increases as we move down the rows in Fig. 5. For all values of Ri_b considered, the cross-stream velocities (streamlines) indicate the presence of channelwide structures. However, the distribution
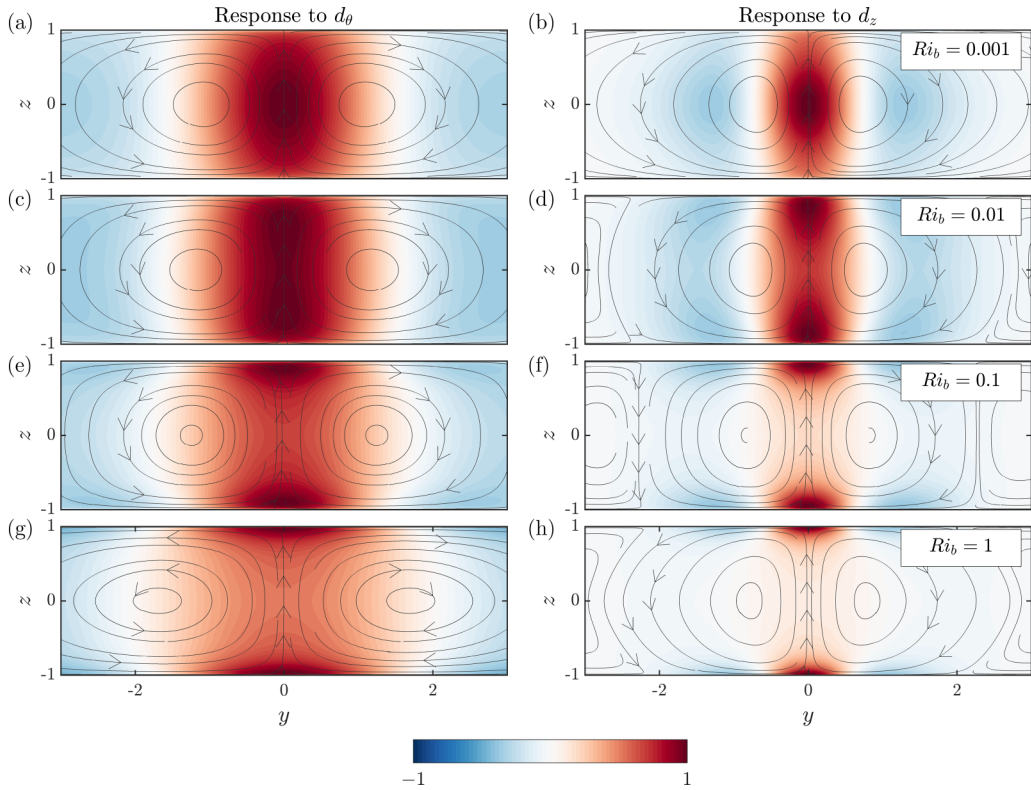
FIG. 5. Normalized (by the maximum) temperature fluctuations θ (contours) and cross-stream velocities v and w (streamlines) obtained as the response of the streamwise constant modes ($k_x = 0$) to an impulse at $(x, y, z, t) = (0, 0, 0, 0)$. (The streamwise velocity u is not shown.) The response is shown at the times $t_c(\text{Ri}_b, z_f)$ computed from Fig. 4. The forcing is either [(a), (c), (e), and (g)] d_θ or [(b), (d), (f), and (h)] d_z. Four cases [(a) and (b)] $\text{Ri}_b = 0.001$, [(c) and (d)] $\text{Ri}_b = 0.01$, [(e) and (f)] $\text{Ri}_b = 0.1$, and [(g) and (h)] $\text{Ri}_b = 1.0$ are considered, with $\text{Re}_b = 10^{4.5}$ and $\text{Pr} = 1$ fixed.

of the temperature field changes with increasing Ri_b. For the case of $\text{Ri}_b = 0.001$ [Fig. 5(a)], the temperature is concentrated at the location of the impulse, i.e., at the channel centerline. At the intermediate case of $\text{Ri}_b = 0.01$ [Fig. 5(c)] we observe that the structure has started to transition to having two peaks in intensity. At the higher Richardson numbers considered, $\text{Ri}_b = 0.1$ and 1.0 [Figs. 5(e) and 5(g)], we see the presence of channelwide structures with two peaks in the intensity of the temperature fluctuations that are concentrated at the channel walls.

Now consider the the response to d_z. The streamlines again indicate the presence of channelwide structures for all the Ri_b considered. As in the case of the response to d_θ, with increasing Ri_b, the temperature field transitions from being centered at the wall-normal height at which the impulse was provided to channelwide structures with two peaks in intensity, one at each wall. However, unlike in the responses to d_θ, the concentration of the temperature fluctuations close to the wall is markedly more pronounced at the higher Richardson numbers of $\text{Ri}_b = 0.1$ and 1.0.

We have seen that the impulse response of the linear model to d_θ and d_z predicts the emergence of channelwide two-peaked intensity features with increasing Ri_b. This is consistent with the DNS results of Pirozzoli *et al.* [25] who observed the presence of large-scale two-peaked intensity features as the influence of buoyancy was increased [see Figs. 5(j) and 5(f) of Pirozzoli *et al.* [25] shown here in Fig. 1]. Figure 5 therefore suggests that, qualitatively, the linear model is able to capture the flow structures that emerge from the competition of shear-driven and buoyancy-driven mechanisms.
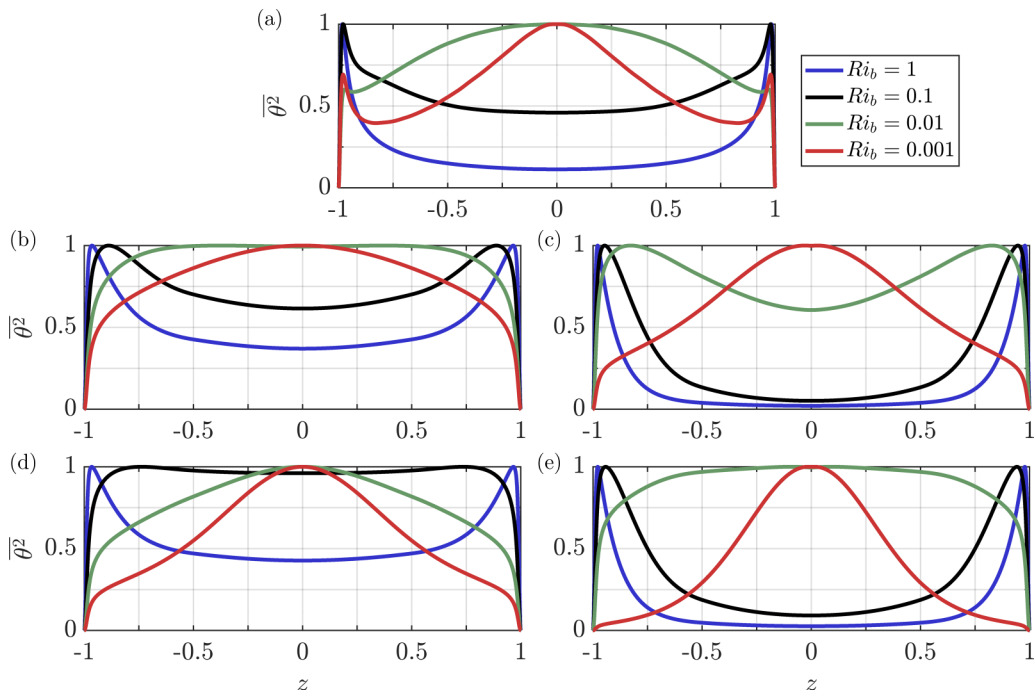
FIG. 6. (a) The normalized profiles of $\overline{\theta^2}$ from DNS (obtained from Pirozzoli *et al.* [25]), and [(b) and (c)] the responses of the streamwise-constant ($k_x = 0$) modes to the impulses (b) d_θ and (c) d_z. Also shown are the responses of the model that includes streamwise-varying modes ($k_x \neq 0$) to the impulses (d) d_θ and (e) d_z. The profiles in (b) and (c) are computed from the fields shown in Fig. 5. The colors indicate the four values of $\mathrm{Ri}_b = 0.001$ (red), 0.01 (green), 0.1 (black), and 1.0 (blue).

However, the responses to d_z at $\mathrm{Ri}_b = 0.1$ and 1.0 display temperature fluctuations that are highly pronounced at the walls, a trend that is not consistent with the flow structures in DNS for which the intensity of temperature fluctuations remains high throughout the channel.

VI. VARIANCE FROM THE IMPULSE RESPONSE

From the trends observed in Fig. 5 we were able to make a qualitative comparison of the large-scale structures from the model with those from DNS. For a more direct comparison, in this section the normalized variance profiles $\overline{\theta^2}$ obtained from the model are compared to DNS. For this purpose, in Fig. 6 we plot the normalized mean profiles of $\overline{\theta^2}$ obtained from DNS and from the impulse responses. The figure includes the four values of Ri_b that were considered in Fig. 5. The profiles in Fig. 6(a) were obtained from the DNS dataset of Pirozzoli *et al.* [25]. The profiles from the model in Figs. 6(b) and 6(c) are computed from the temperature fields shown in Fig. 5. The responses to d_θ and d_z are shown in Figs. 6(b) and 6(c), respectively. Figures 6(d) and 6(e) show the responses that are obtained from the model that includes streamwise-varying modes ($k_x \neq 0$) that will be discussed in Sec. VII (the profiles are included here for ease of comparison later in Sec. VII).

First consider the profiles from DNS in Fig. 6(a). At Richardson numbers $\mathrm{Ri}_b = 0.001$ and 0.01, we see that $\overline{\theta^2}$ peaks at the channel center. We also observe the presence of smaller near-wall peaks at these values of Ri_b. At $\mathrm{Ri}_b = 0.1$ and 1.0 the profiles display two peaks, one at each wall and no peak at the channel centerline. This trend is consistent with the emergence of the quasistreamwise rolls with two peaks in intensity that was observed with increasing Ri_b in Pirozzoli *et al.* [25].

Now consider Fig. 6(b) computed from the response to d_θ. As observed in the DNS, at low Ri_b, the profile of $\overline{\theta^2}$ peaks at the channel center. With increasing Ri_b the profiles transition to having peaks near the walls. This transition is due to the appearance of the two-peaked intensity structures that was observed in Fig. 5. A comparison with Fig. 6(a) shows that this trend is consistent with DNS. However, there are also some important differences. First, the profile corresponding to $Ri = 0.01$ in Fig. 6(b) considerably flattens out close to the channel centerline. From the corresponding contours plots of temperature fluctuations at $Ri_b = 0.01$ in Fig. 5(c), we see that the response has already transitioned to a channelwide feature with two peaks away from the channel centerline, thereby causing this flattening out of the variance profile at this Ri_b. This suggests that the structures from the model transition to the channelwide two-peaked intensity structures at a lower Ri_b than in DNS. Second, the model is not able to capture the near-wall peaks observed in the profiles from DNS at the lowest Richardson numbers of $Ri_b = 0.001$ and 0.01. This may be due to the fact that we have only considered one impulse location of $z_f = 0$ to obtain the variance profiles in Fig. 6(b).

Finally, let us consider Fig. 6(c) which is the variance of the response to d_z. With increasing Ri_b, the profiles of $\overline{\theta^2}$ transition from peaking at the channel center to peaking close to the walls. This is consistent with the trends from DNS in Fig. 6(a). However, as in the case of d_θ, the structures modelled by d_z transition to having two peaks in intensity at a lower Ri_b than in DNS. This trend is more pronounced in Fig. 6(c) in comparison to Fig. 6(b). The near-wall peaks that are seen at lower Ri_b in DNS are also not captured in the response to d_z. Additionally, at $Ri_b = 0.1$ and 1.0 the profiles in Fig. 6(c) are significantly more concentrated close to the wall than in Figs. 6(a) and 6(b). This is consistent with the observations made from Fig. 5(f) in Sec. V. Hence, the response to d_z captures the transition of the structures to the channelwide two-peaked intensity features as in DNS. However, the variance profiles that are obtained do not match DNS as closely as the responses to d_θ.

VII. THE EFFECT OF INCLUDING MODES WITH $k_x \neq 0$

We have so far considered only the streamwise-constant modes when computing the impulse response. In this section we briefly study the influence of including other streamwise wave numbers on the impulse response. Therefore the impulse response is computed for a range of k_x including streamwise-varying ($k_x \neq 0$) modes. The spanwise wave numbers for which the impulse response is computed is kept the same as in the previous sections. We consider a streamwise domain size of 8π, with streamwise Fourier modes varying in integer multiples of $k_{x0} = 1/4$. The streamwise Fourier modes are further truncated such that $-80k_{x0} \leqslant k_x \leqslant 80k_{x0}$ ($\pi/10 \approx 0.31 \leqslant |\lambda_x| < \infty$). For the time instances that we consider here, the excluded wave numbers (that correspond to the smallest structures) have less than 0.1% of the energy of the most energetic Fourier mode in the impulse response.

As performed in Sec. V, here we compare the responses for different Richardson numbers Ri_b. The impulse location is kept fixed at the channel centerline, i.e., $z_f = 0$. The first step is to establish the time $t_c(Ri_b, z_f)$ at which the structures should be compared. To this end, in Figs. 4(c) and 4(d) the normalized kinetic energy norm (13) is plotted with respect to time. This represents the equivalent of Figs. 4(a) and 4(b), this time computed for a range of streamwise wave numbers including streamwise-varying ($k_x \neq 0$) modes. We can therefore compare the trends observed in Figs. 4(c) and 4(d) with those that were observed in Figs. 4(a) and 4(b) in Sec. V.

Let us first consider the response to d_θ. We observe that, in the case of $Ri_b = 0.001$, 0.01, and 0.1, even with the addition of the streamwise-varying ($k_x \neq 0$) modes, the trends in Fig. 4(c) remain largely similar to those seen in Fig. 4(a). The most important difference is that the peaks in Fig. 4(c) occur at slightly earlier times. In the case of $Ri_b = 1.0$, we observe that instead of the monotonic increase of the profile seen in Fig. 4(a), we observe a peak in the profile in Fig. 4(c). This is because, within the time frame considered here, there is the combined effect of the decay in the energy of the streamwise-varying ($k_x \neq 0$) modes and the increase in the energy of the streamwise-constant ($k_x = 0$) modes. Using the trends in Fig. 4(c), we choose the time $t_c(Ri_b, z_f)$ as the time at which the energy

norm (13) peaks. Now let us consider the response to d_z. In this case the trends seen in Figs. 4(d) and 4(b) differ. The norm in Fig. 4(d) does not undergo transient growth and instead monotonically decreases. Hence although the streamwise-constant ($k_x = 0$) modes show transient growth in the streamwise velocity, the combination of the responses across streamwise Fourier modes leads to a monotonic decay of the total energy with time. This is likely due to the different timescales at which each Fourier mode attains its peak energy during its transient response. Using Fig. 4(d) as a guide, we choose a constant time $t_c(\text{Ri}_b, z_f) = 1.0$ to compare the structures when the forcing is in d_z.

We compute the responses to d_θ and d_z at the times $t_c(\text{Ri}_b, z_f)$ computed from Figs. 4(c) and 4(d). The normalized profiles of $\overline{\theta^2}$ obtained from the responses are shown in Figs. 6(d) and 6(e). To analyze the effect of the addition of streamwise-varying modes, the profiles in Figs. 6(d) and 6(e) can be compared to those in Figs. 6(b) and 6(c) (which shows the equivalent profiles computed for the streamwise-constant modes). We observe that for both the forcing d_θ and d_z, the trends observed from the streamwise-varying and streamwise-constant models are similar. In both cases, with increasing Ri_b, the variance profiles transition from peaking at the channel centerline to having two peaks, one located at each of the walls, which is consistent with DNS. Hence the addition of the streamwise-varying modes does not have a significant effect on this trend, and therefore on the emergence of the channelwide two-peaked intensity structures with increasing Ri_b. This indicates that the streamwise-constant modes are the major contributor to the quasistreamwise rolls captured by the linear model. However, the streamwise-varying modes contribute toward an increased variance at the channel center. This can be observed especially in the response to d_θ at $\text{Ri}_b = 0.01$ (green), where the profiles in Figs. 6(d) and 6(e) are in better agreement with DNS than the corresponding profiles in Figs. 6(b) and 6(c). We also observe that, even with the inclusion of streamwise-varying modes, the response to d_z at higher Ri_b is significantly more concentrated at the walls in comparison to DNS.

VIII. THE EFFECT OF IMPULSE LOCATION

In Sec. V we observed that the response of the linear model to impulses in d_θ and d_z captures important features of the large-scale quasistreamwise rolls that appear in unstably stratified channel flows. However, we considered an impulse located at the channel centerline only, i.e., $z_f = 0$. A stratified channel flow is governed by competing shear-driven and buoyancy-driven mechanisms, with the relative importance of these mechanisms varying with wall height. More specifically, as we move away from the wall and toward the channel centerline, the contribution of the buoyancy-driven mechanisms to the turbulent kinetic energy production increases relative to the contribution of the shear-driven mechanisms (Sec. 3.4 of Tennekes and Lumley [63]). It is hence important to consider the effect of the location of the impulse on the response. Therefore, in this section we analyze the response when the impulse is located closer to the wall. We consider a Richardson number of $\text{Ri}_b = 0.1$, for which we observed the emergence of the quasistreamwise rolls in Sec. V. Similar conclusions can also be obtained by considering $\text{Ri}_b = 1.0$ (not shown here). We choose the impulse location to be $z_f = -0.9$ (i.e., 0.1 distance above the lower wall) which, in the case of a turbulent channel flow at similar Re_τ, falls within the log-layer of the flow. In Sec. V we observed that an impulse in the scalar component of the forcing (d_θ) best models the quasistreamwise rolls. Therefore, in the current section we concentrate on the response to d_θ.

As performed in Sec. V we first plot the norm ϕ_{uu} (13) in Fig. 7(a). It is interesting to see that the norm attains its first peak at an earlier time in comparison to the case of $z_f = 0$ [see Fig. 4(a)]. Let us denote this time as t_1. We will also consider the later time t_2 at which the norm attains its second peak. The normalized profiles of $\overline{\theta^2}$ computed from the responses obtained at these times t_1 and t_2 are shown in Fig. 7(b). Considering first the response at the later time t_2 [the dot-dashed line in Fig. 7(b)], we observe that the profile has a peak close to each of the walls, which indicates the presence of the channelwide two-peaked intensity quasistreamiwise rolls. The larger peak at the lower wall (close to the impulse location) suggests that other energetic structures that are localized
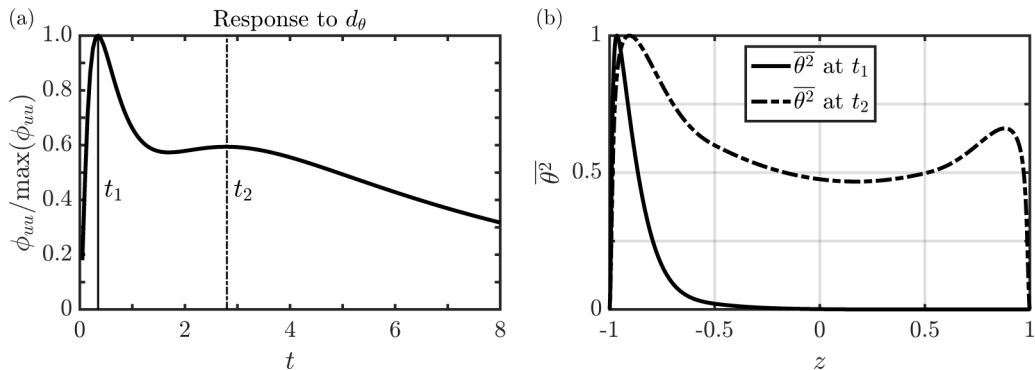
FIG. 7. (a) The norm ϕ_{uu} obtained from the responses of the streamwise-constant modes to the impulse d_θ located at $(x, y, t) = (0, 0, 0)$, plotted as a function of t. The wall-normal location of the impulse is $z_f = -0.9$. The Richardson number is $Ri_b = 0.1$. The two vertical lines indicate the two values of $t_c(Ri_b, z_f)$ used in (b). (b) The profiles of $\overline{\theta^2}$ obtained at the times t_1 and t_2 indicated in (a).

near the impulse location are also present at this time t_2. Now considering the profile obtained at the earlier time t_1 [the solid line in Fig. 7(b)], we see that the profile is localized at the lower wall, i.e., near the impulse location.

From these observations we can conclude that the large-scale quasistreamwise rolls are excited even when the forcing location is moved close to the wall. However, in this case we also observe the presence of other energetic modes that are localized closer to the wall. Such modes were not observed when the impulse was located at the channel centerline (see Sec. V). This suggests that, to model the quasistreamwise rolls using the linearized equations, the impulse location should be taken into account. This is consistent with the properties of this flow, where the relative importance of buoyancy and shear-driven mechanisms changes with wall height.

IX. THE ROLE OF THE RICHARDSON NUMBER AND THE MEAN PROFILES

In this section we consider the question of why the linear model is able to capture the quasistreamwise rolls with their characteristic two-peaked intensity temperature fluctuations? There are two factors that vary within the linear model with increasing Richardson number: (i) the Richardson number itself and therefore the feedback term $-Ri_\tau k^2$ in the matrix A in (5) and (ii) the mean profiles that vary with Ri_τ and are given as input to the linear model (see Fig. 2). Here we consider two modifications of the model so as to isolate the effect of these terms. The impulse responses from these modified models are computed, and then compared to the responses from the full model from Sec. VI. For ease of comparison, the variance of the responses from the full model are reproduced here again in Figs. 8(a) and 8(b), with the responses to d_θ in the first column and the responses to d_z in the second column.

For the first modification of the model we artificially set the feedback term $-Ri_\tau k^2$ in matrix A (5) to zero and thereby isolate the effect of the variation of the mean profiles in A. The times $t_c(Ri_b, z_f)$ at which the responses are compared in this section are again chosen based on the trends of the kinetic energy norm (13) as in Sec. V and for the sake of brevity, the plots of the norm are not shown here. (With the feedback term $-Ri_\tau k^2$ set to zero, the kinetic energy norm of the response to d_θ is zero and we choose a constant $t_c(Ri_b, z_f) = 1.0$ in this case.) The responses obtained from the modified model are shown in Figs. 8(c) and 8(d). From the responses to d_θ in Fig. 8(c) we see that the two-peaked intensity features do emerge, albeit at slightly higher values of Ri_b than in the case of the full model in Fig. 8(a). The shape of the responses to d_z in Fig. 8(d) are indistinguishable from those obtained from the full model in Fig. 8(b), and therefore the responses do not seem to be impacted by the feedback term.
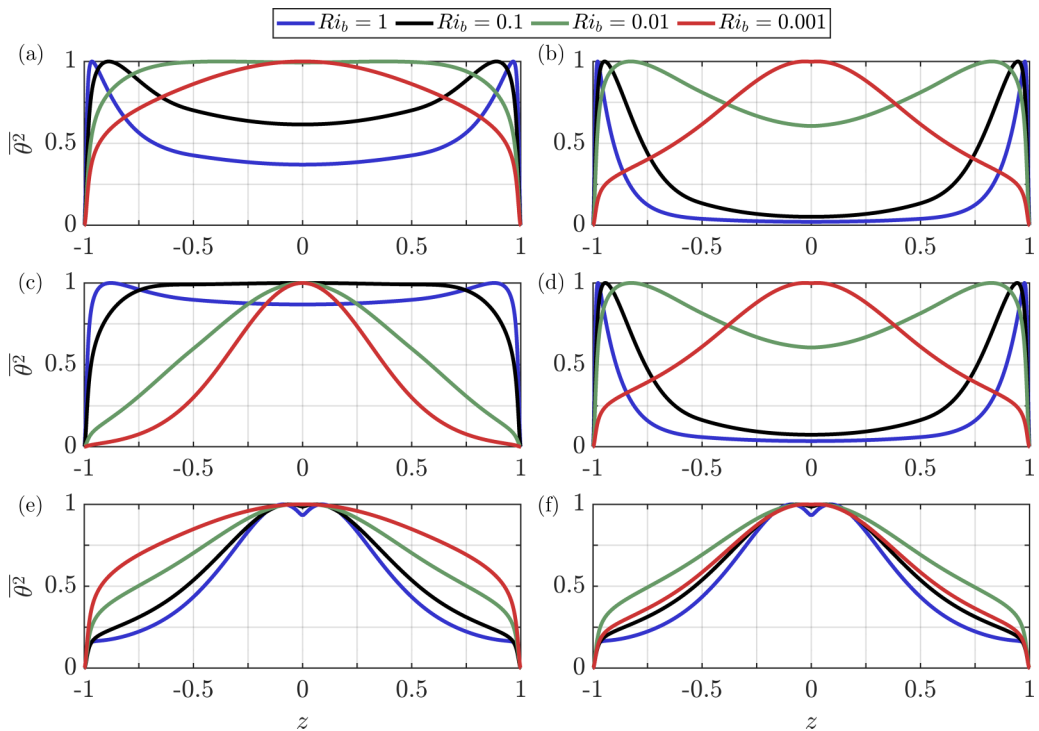
FIG. 8. (a) The normalized profiles of $\overline{\theta^2}$ obtained from the responses of the streamwise-constant ($k_x = 0$) modes to the impulses [(a), (c), and (e)] d_θ and [(b), (d), and (f)] d_z. The responses from [(a) and (b)] the full model as studied in Sec. V, [(c) and (d)] the model where the Richardson number is artificially set to zero, and [(e) and (f)] the model where the mean profiles are artificially taken to be the same as in the case of passive scalar transport are shown. The colors indicate the four values of $\mathrm{Ri}_b = 0.001$ (red), 0.01 (green), 0.1 (black), and 1.0 (blue). The profiles from the full model in (a) and (b) are reproductions of Figs. 4(a) and 4(b), and are shown here for ease of comparison.

Now consider the second modification where we artificially set the mean velocity, temperature, eddy-viscosity, and eddy-diffusivity profiles equal to those in the case of passive scalar transport (obtained from the simulation of Pirozzoli *et al.* [25] with $\mathrm{Ri}_b = 0$). The feedback term $-\mathrm{Ri}_\tau k^2$ increases with Richardson number and therefore in this case, the effect of the variation of the mean profiles is eliminated, and we isolate the effect of the feedback term $-\mathrm{Ri}_\tau k^2$ in $\boldsymbol{A}$. The responses obtained from the modified model are shown in Figs. 8(e) and 8(f). Both from the responses to d_θ and d_z we see that the two-peaked intensity features do not emerge.

These observations suggest that the feedback term in $\boldsymbol{A}$ (5), which is the linear coupling from temperature θ to wall-normal velocity w, does not have a significant influence on the shape of the two-peaked intensity features. Alternatively we can say that the lift-up mechanism, which is the linear coupling from w to streamwise velocity u and temperature θ, has a much more significant role. We can also conclude that the variations in the mean profiles for different Ri_b play a significant role in the existence of the quasistreamwise rolls. This probably makes intuitive sense when considering the mean profiles plotted in Figs. 2(a) and 2(b), especially the mean temperature profile $\overline{\Theta}$. With increasing Ri_b, the profiles of $\overline{\Theta}$ flattens out near the channel centerline, thereby decreasing the magnitude of the wall-normal gradients of mean temperature $d\overline{\Theta}/dz$ in this region. This in turn increases the eddy-diffusivity α_T (2) at the channel centerline, which could cause the responses from the model to stop peaking at the channel centerline (i.e., damps the large structures at the channel centerline) and peak closer to the walls where the value of α_T is lower. This could also

explain why a model with constant α_T does not capture the quasistreamwise rolls, as seen in Appendix A.

X. CONCLUSIONS

In this study we constructed a linearized Navier-Stokes–based model for unstably stratified turbulent channel flows. The nonlinear terms of the equations for velocity (u, v, w) and temperature θ were replaced by an impulsive (localized) disturbance term $\boldsymbol{d} = (d_x, d_y, d_z, d_\theta)$. The responses to these impulses were computed, and the coherent flow structures in the responses were compared to the quasistreamwise rolls observed in the DNS of Pirozzoli *et al.* [25]. The streamwise-constant modes ($k_x = 0$) alone were used to characterize these structures [except in Sec. VII where the effect of adding streamwise-varying ($k_x \neq 0$) modes was discussed]. It was first determined that, to obtain the channelwide modes that are characteristic of these quasistreamwise structures from the linear model, the impulse should either be in the scalar component (d_θ) or the wall-normal component (d_z) of the forcing (Fig. 3). The effect of buoyancy on the large-scale flow structures from the model was then considered by analyzing the response of the linearized equations to d_θ and d_z.

To determine the effect of buoyancy, the responses to an impulse located at the channel centerline ($z_f = 0$) were obtained at different Richardson numbers Ri_b (Figs. 5 and 6). The times at which these structures were compared were determined based on the kinetic energy norm of the responses (the choice of norm does not significantly alter the conclusions derived here). The flow structures from the model were channelwide for all Ri_b considered. As the effect of buoyancy was increased, the temperature fluctuations transitioned from being localized at the impulse location to being channelwide with two peaks in intensity, one at each wall, consistent with the trends in DNS [25]. As a result, the normalized profiles of $\overline{\theta^2}$ obtained from the model agree reasonably well with those obtained from the DNS data [Figs. 6(a) and 6(b)]. The lift-up mechanism, i.e., the linear coupling from the wall-normal velocity w to the streamwise velocity u and temperature θ plays a much more significant role in the emergence of these flow structures than the linear coupling from θ to w. We also found that the shapes of the mean streamwise velocity and temperature profiles (that vary with Ri_b and that are given as input to the model) are important for modeling these flow structures.

The flow structures from the model transition to two-peaked intensity features at lower values of Ri_b than in the case of DNS. We determined that this problem can be resolved by including streamwise-varying modes in the model [Figs. 6(d) and 6(e)]. We also found that, when the impulse is located closer to the wall, in addition to the quasistreamwise rolls, other modes that are localized in the wall-normal direction also become important. Therefore, to model the quasistreamwise rolls using the linearized equations, the location of the impulse should be carefully considered. This is consistent with the properties of unstably stratified turbulent channel flows, where the relative importance of buoyancy-driven and shear-driven mechanisms vary with wall height.

We note that the linear models used in this work require eddy-viscosity and eddy-diffusivity profiles (Sec. A). In the current study we compute these profiles using the mean profiles obtained from DNS. As observed in Sec. II B, computing these profiles from the data obtained from DNS or experiments is challenging. Hence there is the need to obtain a model, such as a modified Cess profile [62], for the case of stratified channel flows. The modified log-law obtained by Scagliarini *et al.* [70] could potentially be useful for this purpose. Any future advancement in this direction will significantly improve our ability to model these flows.

The observations from this study suggest that the linearized Navier-Stokes equations augmented with an eddy-viscosity profile and an eddy-diffusivity profile capture the trends of the quasistreamwise rolls that are observed in turbulent channel flows with unstable stratification [25] reasonably well.
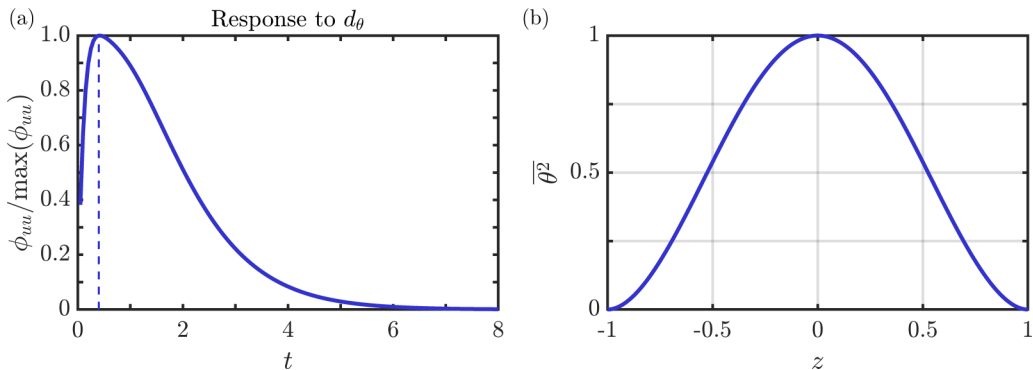
FIG. 9. Response obtained from the linear model with a constant eddy-diffusivity α_T. (a) The norm ϕ_{uu} obtained from the responses of the streamwise-constant modes to the impulse d_θ located at $(x, y, t) = (0, 0, 0)$, plotted as a function of t. The wall-normal location of the impulse is $z_f = 0$ and the Richardson number is $\text{Ri}_b = 1.0$. The vertical line indicates the value of $t_c(\text{Ri}_b, z_f)$ used in (b). (b) The variance profile $\overline{\theta^2}$ obtained at the time $t_c(\text{Ri}_b, z_f)$.

ACKNOWLEDGMENTS

APPENDIX A: LINEAR MODEL WITH CONSTANT EDDY-DIFFUSIVITY

So far we have analyzed the linear model which has its thermal diffusivity augmented with an eddy-diffusivity profile that varies in the wall-normal direction. In this section we briefly consider the effect of using a constant eddy-diffusivity profile α_T. For this purpose, the eddy-diffusivity is kept constant across the channel height, with the constant set equal to the maximum value of the profile obtained in Sec. II B. The wall-normal derivative of the eddy-diffusivity profile is therefore zero. (Other values for this constant eddy-diffusivity profile α_T can be considered. However, as will be shown in this section, this model with a constant α_T does not capture the two-peaked intensity features. We therefore do not consider this question of finding an optimal constant eddy-diffusivity.) The case of Richardson number $\text{Ri}_b = 1.0$, forced using the scalar-component of the forcing d_θ is considered here. For these parameters we observed the emergence of the quasistreamwise rolls in Sec. V.

As performed in Sec. V, we first plot the norm ϕ_{uu} in Fig. 9(a). The time at which the norm peaks is taken as the time $t_c(\text{Ri}_b, z_f)$ at which the variance profile $\overline{\theta^2}$ is computed from the response and plotted in Fig. 9(b). From the variance profile we see that the structure has a peak at the channel centerline, and does not resemble the two-peaked intensity features observed in the case of the model used in Sec. V, which included a wall-normally varying eddy-diffusivity profile. This observation suggests that the wall-normally varying eddy-diffusivity profiles are necessary to model the quasistreamwise rolls of these flows.

APPENDIX B: THE EFFECT OF CHANGING THE NORM

The optimal time $t_c(z_f, \text{Ri})$ at which the responses are plotted in Figs. 5 and 6 depends on the choice of norm. So far we have only considered the kinetic energy norm (13). In this section we look at the effect of changing this choice of norm on the observations made in Sec. V and Sec. VI. We will show that the conclusions derived in those sections are not significantly influenced by the
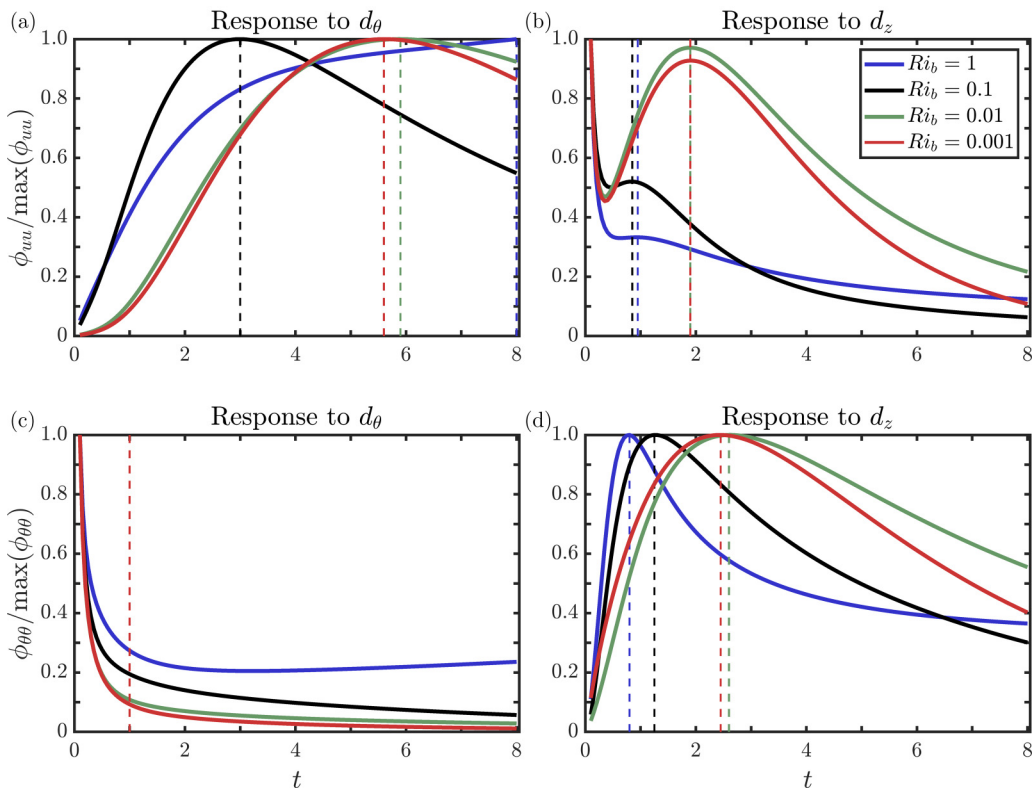
FIG. 10. The norm [(a) and (b)] ϕ_{uu} and [(c) and (d)] $\phi_{\theta\theta}$ obtained from the responses of the stream-wise constant modes to the impulse located at $(x, y, z, t) = (0, 0, 0, 0)$. [(a) and (b)] Reproductions of Figs. 4(a) and 4(b) are shown here for ease of comparison. The norm from the response to [(a) and (c)] d_θ and [(b) and (d)] d_z are plotted as a function of t. The colors indicate the four values of $Ri_b = 0.001$ (red), 0.01 (green), 0.1 (black), and 1.0 (blue). The dashed lines indicate the values of $t_c(Ri_b, z_f)$ used in Fig. 11.

choice of norm. For this purpose we define a new norm $\phi_{\theta\theta}$ as

$$\phi_{\theta\theta} = \int_z \int_{k_x} \int_{k_y} \hat{\theta}(k_x, k_y, z)\hat{\theta}^*(k_x, k_y, z)dk_x dk_y dz. \tag{B1}$$

Before considering this new norm $\phi_{\theta\theta}$, in Figs. 10(a) and 10(b) the kinetic energy norm ϕ_{uu} obtained from the responses to both the scalar component d_θ and the wall-normal component d_z of the forcing, is plotted with respect to time. These are reproductions of Figs. 4(a) and 4(b) in Sec. V, shown here again for ease of comparison. In Fig. 10(c) the new norm $\phi_{\theta\theta}$ (B1) obtained from the responses to d_θ is plotted with respect to time and Fig. 10(d) shows the same for the response to d_z. Here the impulse location is kept fixed at the channel centerline, i.e., $z_f = 0$. The trends of the norm $\phi_{\theta\theta}$ in Figs. 10(c) and 10(d) are different from those observed for ϕ_{uu} in Figs. 10(a) and 10(b). First considering the response to d_θ, unlike the transient growth observed in Fig. 10(a) for ϕ_{uu}, in Fig. 10(c) we observe that $\phi_{\theta\theta}$ shows a decay in energy. A constant value of the time $t_c(z_f, Ri) = 1.0$ is therefore chosen from Fig. 10(c). The norm from the response to d_z in Fig. 10(d) indicates transient growth. This trend is similar to that observed for ϕ_{uu} in Fig. 10(b), although without the initial decay of energy observed in Fig. 10(b). The time $t_c(z_f, Ri)$ from Fig. 10(d) is chosen to be the time at which the norm attains a peak.
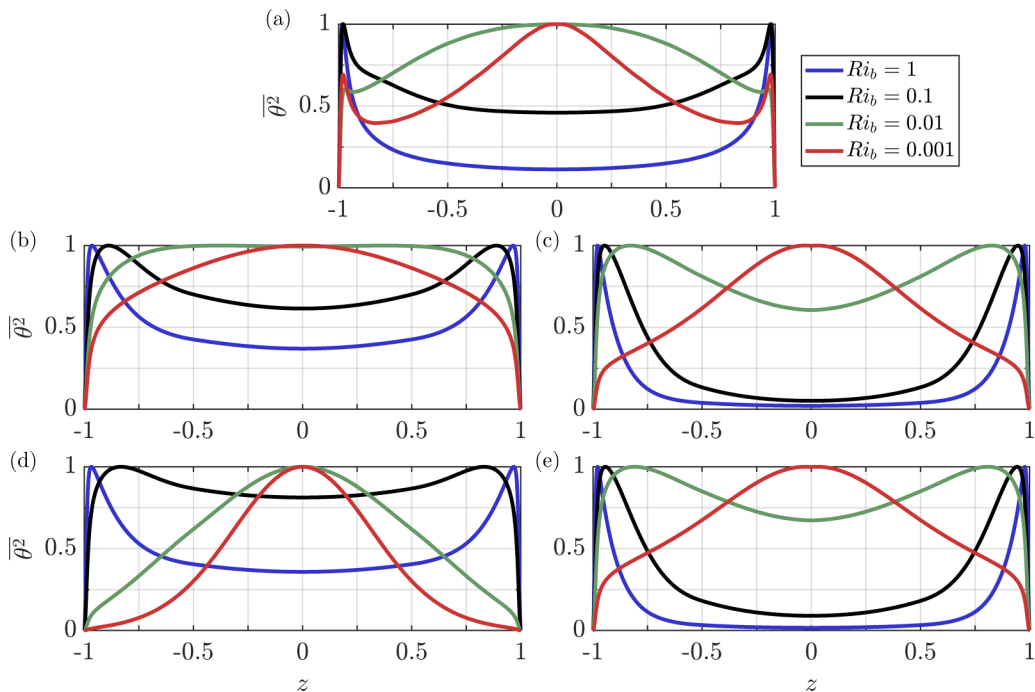
FIG. 11. (a) The normalized profiles of $\overline{\theta^2}$ from DNS (obtained from Pirozzoli *et al.* [25]), and [(b), (c), (d), and (e)] the responses of the streamwise constant modes to the impulses [(b) and (d)] d_θ and [(c) and (e)] d_z. [(b) and (c)] Reproductions of Figs. 6(b) and 6(c) are shown here for ease of comparison. The profiles from the model are computed at the times $t_c(\text{Ri}_b, z_f)$ obtained from [(b) and (c)] Figs. 10(a) and 10(b) using the norm ϕ_{uu} and [(d) and (e)] Figs. 10(c) and 10(d) using the norm $\phi_{\theta\theta}$. The colors indicate the four values of $\text{Ri}_b = 0.001$ (red), 0.01 (green), 0.1 (black), and 1.0 (blue).

We compare the responses to d_θ and d_z across different Ri_b at the $t_c(z_f, \text{Ri})$ computed from Fig. 10. To compare the responses, in Fig. 11 their normalized variance profiles are shown. It should be noted that the only difference between Figs. 11(b) and 11(c) and Figs. 11(d) and 11(e) is the time $t_c(\text{Ri}_b, z_f)$ at which the responses are compared. While Figs. 11(b) and 11(c) are computed at times $t_c(\text{Ri}_b, z_f)$ obtained from Figs. 10(a) and 10(b), Figs. 11(d) and 11(e) are obtained at $t_c(\text{Ri}_b, z_f)$ from Fig. 10(c) and 10(d). [Figures 11(b) and 11(c) are reproductions of Figs. 6(b) and 6(c) in Sec. VI, shown here again for ease of comparison.] The responses to the scalar component of the forcing d_θ are shown in Figs. 11(b) and 11(d) and the responses to the wall-normal component of the forcing d_z are plotted in Figs. 11(c) and 11(e). From the responses to d_θ in Fig. 11(d) we observe that the profiles transition to having two peaks in intensity with increasing Ri_b. This is consistent with Fig. 11(b). However, a slight deviation is observed in the profiles close to the channel centerline, where the variance in Fig. 11(d) is higher in comparison to Fig. 11(b). This is due to the earlier times chosen as $t_c(\text{Ri}_b, z_f)$ from Fig. 10(c), in comparison to those chosen from Fig. 10(a). The responses to d_z in Fig. 11(e), on the other hand, are almost the same as those observed in Fig. 11(c). This is because the $t_c(\text{Ri}_b, z_f)$ chosen for this case from Fig. 10(d) are at later times. Hence the choice of norm does not impact the overall trend of the appearance of the quasistreamwise rolls with increasing effect of buoyancy. However, in the case of an energy decay as in Fig. 10(c), the choice of $t_c(z_f, \text{Ri})$ is more arbitrary than when transient growth is observed [as in Fig. 10(a)]. In this case, if the time chosen is too early, the two-peaked intensity features will not have developed in the flow and therefore the conclusions derived will be impacted.
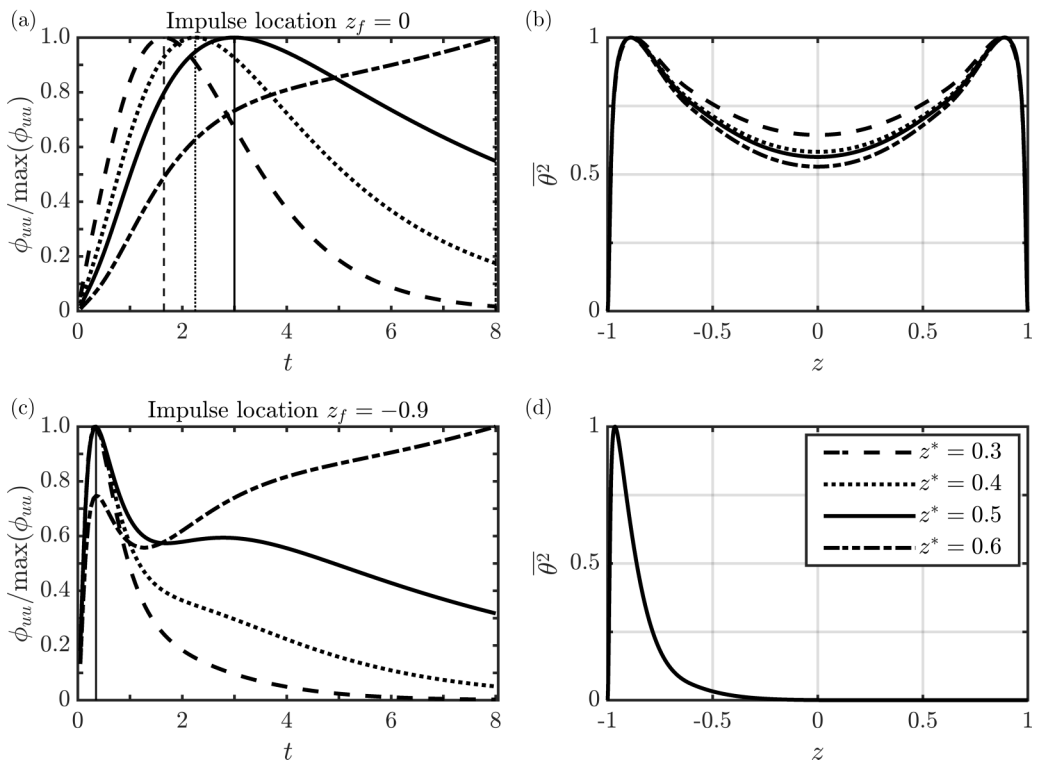
FIG. 12. [(a) and (c)] The norm ϕ_{uu} obtained from the responses to d_θ of the streamwise constant modes to the impulse located at $(x, y, t) = (0, 0, 0)$ at $\mathrm{Ri}_b = 0.1$. The vertical lines indicate the values of $t_c(\mathrm{Ri}_b, z_f)$. [(b) and (d)] The normalized profiles of $\overline{\theta^2}$ obtained from the responses at the obtained $t_c(\mathrm{Ri}_b, z_f)$. Four different values of $z^* = 0.3, 0.4, 0.5,$ and 0.6 are considered for computing the profiles of α_t. The impulse locations are [(a) and (b)] $z_f = 0$ and [(c) and (d)] $z_f = -0.9$.

APPENDIX C: SENSITIVITY TO INTERPOLATION OF EDDY-DIFFUSIVITY

The eddy-viscosity and the eddy-diffusivity profiles used in (1) are computed from the mean profiles obtained from DNS. As discussed in Sec. II B, this introduces the problem of the sensitivity of ν_t and α_t to the noise in the mean profiles. To account for this problem, we use the method of interpolating the profiles used by Cossu *et al.* [18] for the case of a boundary layer. We construct the profiles of ν_t and α_t using the mean profiles obtained from DNS up to some specified wall-normal distance z^* measured from the channel centerline. To obtain the profiles in the region within z^* of the channel centerline we use linear interpolation (see Sec. II B). In this section we discuss the effect of this choice of z^* on the trends discussed. Specifically, we discuss the choice of $z^* = 0.5$ to compute α_t (see Sec. II B). Here we fix $\mathrm{Ri}_b = 0.1$ and concentrate on the response to d_θ, in which case we have seen the emergence of the quasistreamwise rolls in Sec. V. Similar conclusions can be derived at $\mathrm{Ri}_b = 1.0$ as well. We vary the value of z^* used to compute α_t and analyze the changes in the trends observed.

In Figs. 12(a) and 12(c) the normalized ϕ_{uu} profiles shown in Figs. 4(a) and 7(a) are computed again for four different values of z^*. The solid lines corresponding to $z^* = 0.5$ are the same as those shown in Figs. 4(a) and 7(a). Further, three more values of $z^* = 0.3, 0.4,$ and 0.6 are considered. Values of $t_c(\mathrm{Ri}, z_f)$ are chosen from these profiles of the norm, and the variance profiles obtained at these times are shown in Figs. 12(b) and 12(d). The responses to impulses located at $z_f = 0$ and $z_f = -0.9$ are considered in the first and second rows of the figure, respectively. From Fig. 12(a) we

see that as z^* increases, the time at which the norm peaks moves ahead. This time at which the norm peaks is chosen as $t_c(\text{Ri}, z_f)$. At $z^* = 0.6$ the operator $\boldsymbol{A}(k_x, k_y)$ is unstable for some (k_x, k_y) and hence the norm monotonically increases. In this case $t_c(\text{Ri}, z_f)$ is simply chosen to be the maximum time considered in the figure. Now considering Fig. 12(c), although there is great variation in the trends of the norm with increasing z^*, we observe a peak at an early time for all values of z^*. This peak, which occurs at the same t for all values of z^*, is chosen as $t_c(\text{Ri}, z_f)$ in this case.

Now consider the variance profiles computed at these values of $t_c(\text{Ri}, z_f)$ shown in Figs. 12(b) and 12(d). First considering $z_f = 0$ [Fig. 12(b)], the overall trend of obtaining a channelwide structure with a peaks close to each of the two walls is insensitive to the choice of z^*. In the case of $z_f = -0.9$ [Fig. 12(d)] we observe that, again, the choice of z^* does not alter the profiles (the four distinct profiles are not visible in the figure due to their overlap). Hence the value of z^* has a significant impact on the trends of the norm and therefore the choice of $t_c(\text{Ri}, z_f)$. However, for the values of z_f considered in this study, the variance profiles obtained for the different choices of z^* remain similar. From this we conclude that the trends of the channelwide quasistreamwise rolls discussed in this study are reasonably insensitive to the choice of z^*.

---

[1] G. L. Brown and A. S. W. Thomas, Large structure in a turbulent boundary layer, Phys. Fluids **20**, S243 (1977).

[2] K. C. Kim and R. J. Adrian, Very large-scale motion in the outer layer, Phys. Fluids **11**, 417 (1999).

[3] J. Zhou, R. J. Adrian, S. Balachandar, and T. M. Kendall, Mechanisms for generating coherent packets of hairpin vortices in channel flow, J. Fluid Mech. **387**, 353 (1999).

[4] R. J. Adrian, C. D. Meinhart, and C. D. Tomkins, Vortex organization in the outer region of the turbulent boundary layer, J. Fluid Mech. **422**, 1 (2000).

[5] B. Ganapathisubramani, E. K. Longmire, and I. Marusic, Characteristics of vortex packets in turbulent boundary layers, J. Fluid Mech. **478**, 35 (2003).

[6] N. Hutchins, W. T. Hambleton, and I. Marusic, Inclined cross-stream stereo particle image velocimetry measurements in turbulent boundary layers, J. Fluid Mech. **541**, 21 (2005).

[7] C. D. Tomkins and R. J. Adrian, Energetic spanwise modes in the logarithmic layer of a turbulent boundary layer, J. Fluid Mech. **545**, 141 (2005).

[8] D. J. C. Dennis and T. B. Nickels, Experimental measurement of large-scale three-dimensional structures in a turbulent boundary layer. Part 1. Vortex packets, J. Fluid Mech. **673**, 180 (2011).

[9] J. Jiménez, Cascades in wall-bounded turbulence, Annu. Rev. Fluid Mech. **44**, 27 (2012).

[10] N. Hutchins and I. Marusic, Large-scale influences in near-wall turbulence, Phil. Trans. R. Soc. Lond. **365**, 647 (2007).

[11] N. Hutchins and I. Marusic, Evidence of very long meandering features in the logarithmic region of turbulent boundary layers, J. Fluid Mech. **579**, 1 (2007).

[12] J. P. Monty, J. A. Stewart, R. C. Williams, and M. S. Chong, Large-scale features in turbulent pipe and channel flows, J. Fluid Mech. **589**, 147 (2007).

[13] A. J. Smits, B. J. McKeon, and I. Marusic, High-Reynolds number wall turbulence, Annu. Rev. Fluid Mech. **43**, 353 (2011).

[14] M. Guala, S. E. Hommema, and R. J. Adrian, Large-scale and very-large-scale motions in turbulent pipe flow, J. Fluid Mech. **554**, 521 (2006).

[15] B. J. Balakumar and R. J. Adrian, Large- and very-large-scale motions in channel and boundary-layer flows, Phil. Trans. R. Soc. A **365**, 665 (2007).

[16] J. C. Del Álamo and J. Jiménez, Linear energy amplification in turbulent channels, J. Fluid Mech. **559**, 205 (2006).

[17] G. Pujals, M. García-Villalba, C. Cossu, and S. Depardon, A note on optimal transient growth in turbulent channel flows, Phys. Fluids **21**, 015109 (2009).

[18] C. Cossu, G. Pujals, and S. Depardon, Optimal transient growth and very large–scale structures in turbulent boundary layers, J. Fluid Mech. **619**, 79 (2009).

[19] B. J. McKeon and A. S. Sharma, A critical-layer framework for turbulent pipe flow, J. Fluid Mech. **658**, 336 (2010).

[20] Y. Hwang and C. Cossu, Amplification of coherent streaks in the turbulent Couette flow: an input–output analysis at low Reynolds number, J. Fluid Mech. **643**, 333 (2010).

[21] Y. Hwang and C. Cossu, Linear non-normal energy amplification of harmonic and stochastic forcing in the turbulent channel flow, J. Fluid Mech. **664**, 51 (2010).

[22] A. P. Willis, Y. Hwang, and C. Cossu, Optimally amplified large-scale streaks and drag reduction in turbulent pipe flow, Phys. Rev. E **82**, 036321 (2010).

[23] D. F. Gayme, B. J. McKeon, A. Papachristodoulou, B. Bamieh, and J. C. Doyle, A streamwise constant model of turbulence in plane Couette flow, J. Fluid Mech **665**, 99 (2010).

[24] D. F. Gayme, B. J. McKeon, B. Bamieh, A. Papachristodoulou, and J. C. Doyle, Amplification and nonlinear mechanisms in plane Couette flow, Phys. Fluids **23**, 065108 (2011).

[25] S. Pirozzoli, M. Bernardini, R. Verzicco, and P. Orlandi, Mixed convection in turbulent channels with unstable stratification, J. Fluid Mech. **821**, 482 (2017).

[26] A. Blass, X. Zhu, R. Verzicco, D. Lohse, and R. J. A. M. Stevens, Flow organization and heat transfer in turbulent wall sheared thermal convection, J. Fluid Mech **897**, A22 (2020).

[27] J. A. Domaradzki and R. W. Metcalfe, Direct numerical simulations of the effects of shear on turbulent Rayleigh-Bénard convection, J. Fluid Mech **193**, 499 (1988).

[28] A. Garai, J. Kleissl, and S. Sarkar, Flow and heat transfer in convectively unstable turbulent channel flow with solid-wall heat conduction, J. Fluid Mech **757**, 57 (2014).

[29] J. P. Kuettner, The band structure of the atmosphere, Tellus **11**, 267 (1959).

[30] J. P. Kuettner, Cloud bands in the earth's atmosphere: Observations and theory, Tellus **23**, 404 (1971).

[31] D. Etling and R. A. Brown, Roll vortices in the planetary boundary layer: A review, Bound.-Layer Meteorol. **65**, 215 (1993).

[32] S. J. Illingworth, Streamwise-constant large-scale structures in Couette and Poiseuille flows, J. Fluid Mech. **889**, A13 (2020).

[33] K. H. Bech, N. Tillmark, P. H. Alfredsson, and H. I. Andersson, An investigation of turbulent plane Couette flow at low Reynolds numbers, J. Fluid Mech. **286**, 291 (1995).

[34] J. Komminaho, A. Lundbladh, and A. V. Johansson, Very large structures in plane turbulent Couette flow, J. Fluid Mech. **320**, 259 (1996).

[35] D. V. Papavassiliou and T. J. Hanratty, Interpretation of large-scale structures observed in a turbulent plane Couette flow, Int. J. Heat Fluid Flow **18**, 55 (1997).

[36] N. Tillmark and P. H. Alfredsson, Large scale structures in turbulent plane Couette flow, in *Advances in Turbulence VII* (Springer, Berlin, 1998), pp. 59–62.

[37] O. Kitoh, K. Nakabyashi, and F. Nishimura, Experimental study on mean velocity and turbulence characteristics of plane Couette flow: Low-Reynolds-number effects and large longitudinal vortical structure, J. Fluid Mech. **539**, 199 (2005).

[38] T. Tsukahara, H. Kawamura, and K. Shingai, DNS of turbulent Couette flow with emphasis on the large-scale structure in the core region, J. Turbul. **7**, N19 (2006).

[39] O. Kitoh and M. Umeki, Experimental study on large-scale streak structure in the core region of turbulent plane Couette flow, Phys. Fluids **20**, 025107 (2008).

[40] V. Avsarkisov, M. Oberlack, and S. Hoyas, New scaling laws for turbulent Poiseuille flow with wall transpiration, J. Fluid Mech. **746**, 99 (2014).

[41] S. Pirozzoli, M. Bernardini, and P. Orlandi, Turbulence statistics in Couette flow at high Reynolds number, J. Fluid Mech. **758**, 327 (2014).

[42] M. Lee and R. D. Moser, Extreme-scale motions in turbulent plane Couette flows, J. Fluid Mech. **842**, 128 (2018).

[43] J. J. S. Jerome, J. M. Chomaz, and P. Huerre, Transient growth in Rayleigh-Bénard-Poiseuille/Couette convection, Phys. Fluids **24**, 044103 (2012).

[44] E. P. van der Poel, R. Ostilla-Mónico, R. Verzicco, S. Grossmann, and D. Lohse, Logarithmic mean temperature profiles and their connection to plume emissions in turbulent Rayleigh-Bénard convection, Phys. Rev. Lett. **115**, 154501 (2015).

[45] P. Berghout, W. J. Baars, and D. Krug, The large-scale footprint in small-scale Rayleigh–Bénard turbulence, J. Fluid Mech. **911**, A62 (2021).

[46] R. Moarref, A. S. Sharma, J. A. Tropp, and B. J. McKeon, Model-based scaling of the streamwise energy density in high-Reynolds number turbulent channels, J. Fluid Mech. **734**, 275 (2013).

[47] A. S. Sharma and B. J. McKeon, On coherent structure in wall turbulence, J. Fluid Mech. **728**, 196 (2013).

[48] B. F. Farrell and P. J. Ioannou, Perturbation structure and spectra in turbulent channel flow, Theor. Comput. Fluid Dyn. **11**, 237 (1998).

[49] M. Jovanović and B. Bamieh, Modeling flow statistics using the linearized Navier–Stokes equations, in *Proceedings of the 40th IEEE Conference on Decision and Control*, Vol. 5 (IEEE, Los Alamitos, CA, 2001), pp. 4944–4949.

[50] S. T. Dawson, B. J. McKeon, and T. Saxton-Fox, Modeling passive scalar dynamics in wall-bounded turbulence using resolvent analysis, in *Proceedings of the AIAA Fluid Dynamics Conference* (AIAA, Reston, VA, 2018), p. 4042.

[51] T. Saxton-Fox, Coherent structures, their interactions, and their effects on passive scalar transport and aero-optic distortion in a turbulent boundary layer, Ph.D. thesis, California Institute of Technology, 2018.

[52] T. Saxton-Fox and B. J. McKeon, Modeling momentum and scalar transport in a wall-bounded turbulent flow, in *Proceedings of the 10th International Symposium on Turbulence and Shear Flow Phenomena* (Begel House Inc., Chicago, IL, 2017).

[53] M. A. Ahmed, H. J. Bae, A. F. Thompson, and B. J. McKeon, Resolvent analysis of stratification effects on wall-bounded shear flows, Phys. Rev. Fluids **6**, 084804 (2021).

[54] P. Huerre and P. A. Monkewitz, Absolute and convective instabilities in free shear layers, J. Fluid Mech. **159**, 151 (1985).

[55] M. R. Jovanović and B. Bamieh, The spatio-temporal impulse response of the linearized Navier-Stokes equations, in *Proceedings of the 2001 American Control Conference*, Vol. 3 (IEEE, Los Alamitos, CA, 2001), pp. 1948–1953.

[56] M. R. Jovanović, Modeling, analysis, and control of spatially distributed systems, Ph.D. thesis, University of California at Santa Barbara, Dept. of Mechanical Engineering, 2004.

[57] G. Hariharan, M. R. Jovanović, and S. Kumar, Amplification of localized body forces in channel flows of viscoelastic fluids, J. Non-Newtonian Fluid Mech. **260**, 40 (2018).

[58] P. Luchini, M. Quadrio, and S. Zuccher, The phase-locked mean impulse response of a turbulent channel flow, Phys. Fluids **18**, 121702 (2006).

[59] A. R. Codrignani, Impulse response in a turbulent channel flow, Ph.D. thesis, Politecnico Milano, 2014.

[60] S. B. Vadarevu, S. Symon, S. J. Illingworth, and I. Marusic, Coherent structures in the linearized impulse response of turbulent channel flow, J. Fluid Mech. **863**, 1190 (2019).

[61] W. C. Reynolds and A. K. M. F. Hussain, The mechanics of an organized wave in turbulent shear flow. Part 3. Theoretical models and comparisons with experiments, J. Fluid Mech. **54**, 263 (1972).

[62] R. D. Cess, A survey of the literature on heat transfer in turbulent tube flow, Westinghouse Research Report No. 8-0529-R24, 1958 (unpublished).

[63] H. Tennekes and J. L. Lumley, *A First Course in Turbulence* (MIT Press, Cambridge, MA, 1972).

[64] P. J. Schmid and D. S. Henningson, *Stability and Transition in Shear Flows* (Springer, Berlin, 2001).

[65] K. S. Gage and W. H. Reid, The stability of thermally stratified plane Poiseuille flow, J. Fluid Mech. **33**, 21 (1968).

[66] S. J. Illingworth, J. P. Monty, and I. Marusic, Estimating large-scale structures in wall turbulence using linear models, J. Fluid Mech. **842**, 146 (2018).

[67] P. Morra, O. Semeraro, D. S. Henningson, and C. Cossu, On the relevance of reynolds stresses in resolvent analyses of turbulent wall-bounded flows, J. Fluid Mech. **867**, 969 (2019).

[68] A. P. Siebesma, P. M. M. Soares, and J. Teixeira, A combined eddy-diffusivity mass-flux approach for the convective boundary layer, J. Atmos. Sci. **64**, 1230 (2007).

[69] B. R. Kusse and E. A. Westwig, *Mathematical Physics: Applied Mathematics for Scientists and Engineers* (John Wiley & Sons, New York, 2010).

[70] A. Scagliarini, H. Einarsson, Á. Gylfason, and F. Toschi, Law of the wall in an unstably stratified turbulent channel flow, J. Fluid Mech. **781**, R5 (2015).